ELSEVIER

Contents lists available at ScienceDirect

### Additive Manufacturing

journal homepage: www.elsevier.com/locate/addma



#### Research paper

# Additive manufacturing of stiff and strong structures by leveraging printing-induced strength anisotropy in topology optimization

Rahul Dev Kundu<sup>a</sup>, Xiaojia Shelly Zhang<sup>a,b,\*</sup>

- a Department of Civil and Environmental Engineering, University of Illinois Urbana-Champaign, 205 North Mathews Ave, Urbana, IL 61801, USA
- b Department of Mechanical Science and Engineering, University of Illinois Urbana-Champaign, USA



Keywords:
Anisotropic strength
Tsai-Wu criterion
AM-oriented topology optimization
Infill optimization
Process-induced anisotropy
Material extrusion 3D printing



Anisotropy in additive manufacturing (AM), particularly in the material extrusion process, plays a crucial role in determining the actual structural performance, including the stiffness and strength of the printed parts. Unless accounted for, anisotropy can compromise the objective performance of topology-optimized structures and allow premature failures for stress-sensitive design domains. This study harnesses processinduced anisotropy in material extrusion-based 3D printing to design and fabricate stiff, strong, and lightweight structures using a two-step framework. First, an AM-oriented anisotropic strength-based topology optimization formulation optimizes the structural geometry and infill orientations, while assuming both anisotropic (i.e., transversely isotropic) and isotropic infill types as candidate material phases. The dissimilar stiffness and strength interpolation schemes in the formulation allow for the optimized allocation of anisotropic and isotropic material phases in the design domain while satisfying their respective Tsai-Wu and von Mises stress constraints. Second, a suitable fabrication methodology realizes anisotropic and isotropic material phases with appropriate infill density, controlled print path (i.e., infill directions), and strong interfaces of dissimilar material phases. Experimental investigations show up to 37% improved stiffness and 100% improved strength per mass for the optimized and fabricated structures. The anisotropic strength-based optimization improves load-carrying capacity by simultaneous infill alignment along the stress paths and topological adaptation in response to high stress concentration. The adopted interface fabrication methodology strengthens comparatively weaker anisotropic joints with minimal additional material usage and multi-axial infill patterns. Furthermore, numerically predicted failure locations agree with experimental observations. The demonstrated framework is general and can potentially be adopted for other additive manufacturing processes that exhibit anisotropy, such as fiber composites.

#### 1. Introduction

Topology optimization [1,2] is a computational method used for optimizing material usage in a design domain while satisfying a set of constraints. The resulting optimized designs often have complex organic shapes that are difficult to fabricate with traditional manufacturing processes such as machining. To overcome this challenge, additive manufacturing (AM) is often used in combination with topology optimization for demonstration, experimental validation, and real-world application of optimized structures [3].

One of the notable characteristics of additively manufactured structures is their material anisotropy, which can be intrinsic or process-induced. Intrinsic anisotropy arises from the inherent direction-dependent properties of the used materials, such as the high stiffness and

strength of fiber-reinforced composite materials along the fiber orientation. Process-induced anisotropy usually occurs due to the manufacturing process, primarily because of insufficient or nonuniform inter-layer bonding owing to layer-by-layer manufacturing strategy for most AM processes. In addition to this out-of-plane build anisotropy, in-plane anisotropy can also occur from the extrusion of material from a nozzle in the case of fused deposition modeling (FDM) printing. In this case, high stiffness and strength are generally observed along the extrusion or infill direction [4–11]. The inclusion of material anisotropy, either intrinsic or process-induced, is critical for additive manufacturing of topology optimized designs, as inaccurate representation of material properties in the optimization formulation may lead to worse objective function values and constraint violations for the fabricated structures.

E-mail address: zhangxs@illinois.edu (X.S. Zhang).

<sup>\*</sup> Corresponding author at: Department of Civil and Environmental Engineering, University of Illinois Urbana-Champaign, 205 North Mathews Ave, Urbana, IL 61801, USA.

The importance of anisotropy in topology optimization for additive manufacturing is widely discussed in literature [12,13].

The additively manufactured anisotropic parts from material extrusion printing are typically stiffer and stronger in the longitudinal direction than in the transverse direction, where the longitudinal direction is determined by the orientation of the fiber or the print path [14]. To exploit this advantage, several studies have attempted to align reinforcing fibers and print paths along the principal stress to improve mechanical performance, i.e., stiffness and strength, of the fabricated structures [15-21]. However, these approaches often overlook the need for simultaneous structural geometry/topology optimization for strength and therefore, may require further print-path control to prevent printing overlap in regions with stress concentrations. Most studies that involve topology optimization with anisotropic materials for additive manufacturing consider only constitutive anisotropy without explicitly considering anisotropic strength [22-27]. While some approaches demonstrate an increase in strength while optimizing structures for increased stiffness [16-18,28,29], they do not ensure the prevention of high stress concentration-induced material failure for a prescribed load. Premature failure prevention with stress-based topology optimization is mostly discussed and demonstrated for isotropic failure criteria for the candidate materials. These studies indicate that incorporating material strength in the optimization formulation may enhance structural strength, i.e., load carrying capacity per unit volume, by suitable changes in geometry (e.g., with von Mises stress limits [30,31]) and efficient use of tension-compression asymmetry (e.g., with Drucker-Prager yield criterion [32-34]). However, the commonly used von Mises and other direction-independent failure/yield criteria-based topology optimization may not be suitable for additive manufacturing involving material anisotropy. Experimental investigation with von Mises stress-constrained topology optimization and Fused Deposition Modeling (FDM) additive manufacturing [35] also confirms that strength of optimized and fabricated structure varies with deposition path direction and build direction, which supports the necessity of using anisotropic strength criterion.

Several studies incorporate strength anisotropy in additive manufacturing and find optimized build orientation for a given structure, without optimizing topology, by considering anisotropy either along and perpendicular to the build-plane [36,37] or along and perpendicular to the infill or print path [16]. On the other hand, some studies optimize topology for a given build orientation while accounting for strength anisotropy along and perpendicular to the build direction. For example, [38] considers anisotropic tensile strength for lattice materials and aligns lattice members along the principle stresses. Some recent studies consider Tsai-Wu [39] and Hoffman [40] failure criteria in topology optimization framework to account for both tension and compression anisotropy for differential strengths along and perpendicular to print plane. These strategies may be sufficiently effective for AM processes with relatively direction-independent in-plane material properties, such as powder bed fusion, when assuming a constant build direction. However, for AM processes with significant in-plane anisotropy, like in material extrusion, such strategies would not harness the advantage from freely optimized in-plane print-path or infill orientations. Except for a few recent studies [41,42], a general methodology that harnesses anisotropic strength with optimized structural geometry and in-plane fiber or print-path orientations, especially in additive manufacturing with experimental evidence, is currently underdeveloped.

This study demonstrates how material anisotropy induced during additive manufacturing (AM), specifically in material extrusion 3D printing, can be leveraged to design stiff, strong, and lightweight structures by simultaneously optimizing the design geometry and the orientation of in-plane infill directions using an anisotropic strength-based topology optimization framework. The methodology assumes plane stress problems, and incorporates transversely isotropic stiffness and strength to account for in-plane anisotropy from material extrusion paths. First, several stress-sensitive design domains are optimized with

a unique strength-based topology optimization that considers both direction-dependent and -independent stiffness and strengths of dissimilar candidate material phases. The formulation minimizes the weighted sum of compliance and relative material mass while satisfying Tsai-Wu and von Mises stress constraints for candidate anisotropic and isotropic material phases, respectively, to provide high stiffness and strength per material usage. Then the process-induced anisotropy from material extrusion 3D printing is utilized to fabricate the optimized designs with anisotropic and isotropic parts. Suitable infill density and interface fabrication strategy are adopted to further facilitate the high stiffnessand strength-to-mass ratios in the fabricated structures. The fabricated structures are experimentally investigated for their stiffness, strength, and material usage to demonstrate the advantages of the proposed design optimization and fabrication methodology. The major contribution of this work is proposing an overall methodology to design and manufacture stiff and strong structures with material extrusion additive manufacturing by accounting for printing-induced strength anisotropy, which involves (a) simultaneous optimization of both topology and orthotropy/anisotropy direction with the consideration of printinginduced strength anisotropy, (b) realization and characterization of anisotropic/isotropic infill, (c) proposing a strong, multi-axial interface fabrication suitable for topology optimized anisotropic structures, and (d) experimental evidence of increased stiffness and strength compared to some conventional fabrication approaches. While this study focuses on material extrusion AM, the proposed methodology may also be adapted to optimize build directions for other AM processes with dominant out-of-plane build anisotropy, such as powder bed fusion, by enabling multicomponent topology optimization [43,44] and modular fabrication, where longitudinal and transverse directions can be represented by directions along and perpendicular to the print-plane. Therefore, this work contributes towards the realization and demonstration of stiff, strong, and lightweight structures with optimized use of process-induced anisotropy in additive manufacturing. The remainder of the paper is as follows. Section 2 presents the adopted topology optimization framework, fabrication details of optimized designs using material extrusion 3D printing, and characterized stiffness and strength parameters for the used anisotropic and isotropic material phases. Section 3 discusses the experimental setup and the test results. Section 4 summarizes the observations and discusses the limitations and possible future directions.

#### 2. Material and methods

This section presents the design optimization and fabrication details, considering anisotropy in stiffness and strength induced by the printing process in material extrusion 3D printing. Section 2.1 includes the topology optimization framework that generates stiff, strong, and lightweight optimized designs using both anisotropic and isotropic material phases. Section 2.2 presents the manufacturing details for anisotropic and isotropic material parts along with their interfaces. Section 2.3 summarizes the characterized stiffness and strength properties of the different material phases, which are then used for the design optimization examples presented in Section 3.

### 2.1. Strength-based topology optimization with anisotropic and isotropic parts

This study employs the anisotropic strength-based topology optimization framework [45] to generate optimized designs for additive manufacturing that are stiff, strong, and lightweight. The framework uses a multimaterial topology optimization approach, where the candidate material phases include an anisotropic (i.e., transversely isotropic) material phase with different available longitudinal directions and an isotropic material phase. A brief description of the framework is presented below, including (a) the multimaterial design parameterization with anisotropic and isotropic material phases along with their dissimilar stiffness and strength interpolation schemes, and (b) the Augmented-Lagrangian based optimization formulation considering many local anisotropic and isotropic stress constraints.

#### 2.1.1. Design parameterization and multimaterial interpolation schemes

This study uses a two-field multimaterial design parameterization scheme [46,47], where the design density variable  $\rho$  characterizes the structural geometry, and the design material variables  $\xi^{(k)}$ , k = $1, \ldots, N_{\varepsilon}$ , characterize the anisotropic and isotropic material phases in the design. For each element e in a discretized design domain, (a) solid and void regions are characterized by  $\bar{\rho}_e$  taking values of 1 and 0, respectively, where  $\bar{\rho}$  is the physical density variable obtained using filter [48–50] and Heaviside projection [51] on  $\rho$ , and (b) the presence and absence of material phase i is characterized by  $\bar{m}_e^{(i)}$  taking values 1 and 0, respectively, where  $\bar{\mathbf{m}}^{(i)}$ ,  $i = 1, ..., N_m$ , are the physical material variables obtained using filter, Heaviside projection, and a tailored HSP mapping [52] on  $\xi^{(k)}, k = 1, ..., N_{\xi}$ . The filter and Heaviside projection on both design variables facilitate regularized, mesh-independent, and discrete optimized designs [50,53]. The tailored HSP mapping for material variables enforces the condition  $\sum_{i=1}^{N_m} (\bar{m}_e^{(i)}) = 1$  to represent a physical structure, where candidate material i occupies  $\bar{m}_e^{(i)}$  portion in element e. More details regarding the filter, projection, and tailored HSP mapping used in this study are provided in Appendix A. Note that while  $\bar{\rho}_a$  and  $\bar{m}_a^{(i)}$  take binary values of 0 and 1 for an optimized design, they may take intermediate values between 0 and 1 during the optimization steps for an intermediate design. Such intermediate values of  $\bar{\rho}_e$  and  $\bar{m}_e^{(i)}$  necessitate the interpolation of dissimilar material properties, i.e., stiffness and strength, to characterize the mechanical behavior of intermediate designs during optimization.

For stiffness interpolation, a SIMP-based [46,54] multimaterial stiffness interpolation scheme [47,55,56] is adopted. The interpolated stiffness tensor  $\mathbb{C}_e^{(\xi)}$  is expressed as

$$\mathbb{C}_{e}^{(\xi)}(\bar{\rho}_{e}, \bar{m}_{e}^{(1)}, \dots, \bar{m}_{e}^{(N_{m})}) = \left[\varepsilon + (1 - \varepsilon)\bar{\rho}_{e}^{p_{\rho}}\right] \sum_{i=1}^{N_{m}} (\bar{m}_{e}^{(i)})^{p_{\xi}} \mathbb{C}^{(i)}, \tag{1}$$

where  $\mathbb{C}^{(i)}$  is the stiffness tensor of material phase i,  $p_{\rho}$  and  $p_{\xi}$  are the density and material variable penalization parameters, respectively, and  $\varepsilon$  is a sufficiently small number to prevent numerical singularity. For an anisotropic (i.e., transversely isotropic) material phase, the matrix form of the stiffness tensor  $\mathbb{C}^{(i)}$  for a 2D plane stress problem is obtained from

$$\mathbf{C}^{(i)}|_{i=\text{aniso}} = T^{-1}(\boldsymbol{\theta}^{(i)}) \begin{bmatrix} \frac{E_{11}}{1 - v_{12}v_{21}} & \frac{v_{12}E_{22}}{1 - v_{12}v_{21}} & 0\\ \frac{v_{12}E_{22}}{1 - v_{12}v_{21}} & \frac{E_{22}}{1 - v_{12}v_{21}} & 0\\ 0 & 0 & G_{12} \end{bmatrix} T^{-T}(\boldsymbol{\theta}^{(i)}),$$

$$i = 1, \dots, N_{\theta}, \tag{2}$$

where  $E_{11}$  and  $E_{22}$  are the elastic moduli along the longitudinal and transverse directions, respectively,  $v_{12}$  is the Poisson's ratio with respect to the longitudinal direction, and  $G_{12}$  is the shear modulus. The 2D plane stress transformation matrix  $T(\theta^{(i)})$  corresponding to longitudinal direction  $\theta^{(i)}$  of candidate anisotropic material phase i is given by

$$T(\theta) = \begin{bmatrix} \cos^2(\theta) & \sin^2(\theta) & 2\sin(\theta)\cos(\theta) \\ \sin^2(\theta) & \cos^2(\theta) & -2\sin(\theta)\cos(\theta) \\ -\sin(\theta)\cos(\theta) & \sin(\theta)\cos(\theta) & \cos^2(\theta) - \sin^2(\theta) \end{bmatrix}. \tag{3}$$

For an isotropic material phase, the matrix form of the stiffness tensor  $\mathbb{C}^{(i)}$  for a 2D plane stress problem is simply obtained as

$$\mathbf{C}^{(i)}|_{i=\mathrm{iso}} = \frac{E_{\mathrm{iso}}}{1 - v_{\mathrm{iso}}^2} \begin{bmatrix} 1 & v_{\mathrm{iso}} & 0\\ v_{\mathrm{iso}} & 1 & 0\\ 0 & 0 & \frac{1 - v_{\mathrm{iso}}}{2} \end{bmatrix},\tag{4}$$

where  $E_{\rm iso}$  and  $v_{\rm iso}$  are elastic modulus and Poisson's ratio, respectively. For dissimilar strength interpolation, this study adopts an anisotropic yield function interpolation scheme that simultaneously considers anisotropic (i.e., transversely isotropic) Tsai–Wu and isotropic von Mises yield criteria. The SIMP-like interpolation for multimaterial yield function  $f_e^{(\xi)}$  is obtained as [34],

$$f_e^{(\xi)}(\bar{m}_e^{(1)}, \dots, \bar{m}_e^{(N_m)}, \sigma_e^{(1)}, \dots, \sigma_e^{(N_m)}) = \sum_{i=1}^{N_m} (\bar{m}_e^{(i)})^{p_{f_{\xi}}} f^{(i)}(\sigma_e^{(i)}), \tag{5}$$

where  $\sigma_e^{(i)} := \mathbb{C}^{(i)} \epsilon_e$  and  $f^{(i)}(\sigma)$  are the stress state and yield function corresponding to ith candidate material phase for element e,  $\epsilon_e$  is the strain field for element e, and  $p_{f_\xi}$  is a penalization parameter. For an anisotropic material phase, the yield function  $f^{(i)}(\sigma^{(i)})$  is obtained from the load factor based Tsai–Wu yield criterion as

$$f^{(i)}(\sigma^{(i)})|_{i=\text{aniso}} = \eta^{(\text{tw})}(\sigma^{(i)}, \theta^{(i)})$$

$$= \frac{2A(\sigma^{(i)}, \theta^{(i)})}{\sqrt{B^2(\sigma^{(i)}, \theta^{(i)}) + 4A(\sigma^{(i)}, \theta^{(i)}) - B(\sigma^{(i)}, \theta^{(i)})}} \le 1,$$
 (6)

where  $\eta^{(\text{tw})}(\sigma,\theta)$  is the load factor [39,57], and  $A(\sigma,\theta) = \max\left(F_{11}\sigma_{11}^2 + F_{22}\sigma_{22}^2 + F_{66}\sigma_{12}^2 + F_{12}\sigma_{11}\sigma_{22}, 10^{-12}\right)$ , and  $B(\sigma,\theta) = F_1\sigma_{11} + F_2\sigma_{22}$  are the quadratic and linear parts of the actual Tsai–Wu yield criterion [58], which is expressed for a 2D plane stress problem as

$$f^{(\text{tw})}(\boldsymbol{\sigma},\boldsymbol{\theta}) = F_{11}\sigma_{11}^2 + F_{22}\sigma_{22}^2 + F_{66}\sigma_{12}^2 + F_{12}\sigma_{11}\sigma_{22} + F_{1}\sigma_{11} + F_{2}\sigma_{22} \leq 1, \ \ (7)$$

where  $\sigma_{11}$ ,  $\sigma_{22}$ , and  $\sigma_{12}$  are the in-plane stress components with respect to the longitudinal direction. The coefficients in (7) are given by

$$F_{1} = \frac{1}{X_{t}} - \frac{1}{X_{c}}, \quad F_{2} = \frac{1}{Y_{t}} - \frac{1}{Y_{c}},$$

$$F_{11} = \frac{1}{X_{t} \cdot X_{c}}, \quad F_{22} = \frac{1}{Y_{t} \cdot Y_{c}},$$

$$F_{66} = \frac{1}{S \cdot S}, \quad F_{12} = -0.5\sqrt{F_{11}F_{22}},$$
(8)

where  $X_t$  and  $X_c$  denote the tension and compression strengths along the longitudinal direction, respectively,  $Y_t$  and  $Y_c$  denote the tension and compression strengths along the transverse direction, respectively, and S denotes the shear strength. For an isotropic material phase, the yield function  $f^{(i)}(\sigma^{(i)})$  is the von Mises yield criterion [59] expressed as

$$f^{(i)}(\sigma^{(i)})|_{i=iso} = f^{(vm)}(\sigma^{(i)}) = \frac{\sigma_{vm}(\sigma^{(i)})}{\bar{\sigma}_{iso}} \le 1,$$
 (9)

where  $\sigma_{\rm vm}(\sigma)$  is the von Mises stress, and  $\bar{\sigma}_{\rm iso}$  is the von Mises stress limit for the isotropic material phase.

Notice that, the load factor based Tsai–Wu criterion (6) reduces to von Mises criterion (9) when  $X_t = Y_t = X_c = Y_c = \sqrt{3}S = \bar{\sigma}_{\rm iso}$ . Hence, this load factor based Tsai–Wu criterion (6) is used in the yield function interpolation scheme (5) instead of the actual Tsai–Wu criterion (7) for a consistent and uniform interpolation [45] with the von Mises criterion (9).

#### 2.1.2. Optimization formulation

Based on the multimaterial design parameterization and material interpolation schemes, an optimized formulation is presented to minimize the weighted sum of compliance and mass of the structure. This objective function aims to obtain a lightweight design with sufficient stiffness. The effect of different compliance and mass weights in the objective function is briefly discussed in Appendix C. Polynomial vanishing stress constraints with accelerated convergence properties [31, 33] are used to satisfy individual yield criteria of anisotropic and isotropic material phases in the optimized design. Minimizing compliance and mass together results in a lightweight and stiff structure, whereas the stress constraints enhance the overall structural strength by preventing premature material failure. The topology optimization problem is formulated as

$$\begin{split} \min_{\rho,\xi^{(1)},\dots,\xi^{(N_{\xi})}} & \quad J\left(\rho,\xi^{(1)},\dots,\xi^{(N_{\xi})}\right) = wC + (1-w) \sum_{i=1}^{N_m} \hat{\gamma}_i V_i, \\ \text{s.t.} & \quad g_e\left(\rho,\xi^{(1)},\dots,\xi^{(N_{\xi})},\mathbf{U}\right) = \left[\varepsilon + (1-\varepsilon)\bar{\rho}_e(\rho)^{\rho_\rho}\right] \\ & \quad \left(f_e^{(\xi)}(\xi^{(1)},\dots,\xi^{(N_{\xi})},\mathbf{U}) - 1\right) \\ & \quad \left(\left(f_e^{(\xi)}(\xi^{(1)},\dots,\xi^{(N_{\xi})},\mathbf{U}) - 1\right)^2 + 1\right) \leq 0, \\ & \quad e = 1,\dots,N_e, \\ & \quad \rho_e \in [0,1], \\ & \quad e = 1,\dots,N_e, \\ & \quad \xi_e^{(k)} \in [0,1], \\ & \quad e = 1,\dots,N_e, \quad k = 1,\dots,N_{\xi}, \\ \end{aligned} \end{split}$$
 with: 
$$\quad \mathbf{K}\left(\rho,\xi^{(1)},\dots,\xi^{(N_{\xi})}\right) \mathbf{U} = \mathbf{F}^{\text{ext}}, \end{split}$$

where  $C = (\mathbf{F}^{\text{ext}})^T \mathbf{U}(\boldsymbol{\rho}, \boldsymbol{\xi}^{(1)}, \dots, \boldsymbol{\xi}^{(N_{\xi})}) / C^*$  is the normalized end-compliance with  $C^*$  being the end-compliance of uniform initial guess,  $V_i =$  $\sum_{e=1}^{N_e} \left( \bar{\rho}_e(\boldsymbol{\rho}) \bar{m}_e^{(i)}(\boldsymbol{\xi}^{(1)}, \dots, \boldsymbol{\xi}^{(N_\xi)}) v_e \right) / \sum_{e=1}^{N_e} v_e \text{ is the structural volume fraction}$ tion occupied by material phase i with  $v_a$  being the volume of element  $e, \hat{\gamma}_i = \gamma_i / \max(\gamma_i)$  where  $\gamma_i \in [0, 1]$  is the infill density for the material phase  $i, w \in [0,1]$  is a weight factor for the compliance term in the objective,  $f_e^{(\xi)}(\xi^{(1)}, \dots, \xi^{(N_{\xi})}, U(\rho, \xi^{(1)}, \dots, \xi^{(N_{\xi})}))$  is the interpolated yield function value (5) associated with element e,  $\mathbf{K}\left(\rho, \boldsymbol{\xi}^{(1)}, \dots, \boldsymbol{\xi}^{(N_{\xi})}\right)$  is the global stiffness matrix obtained from the stiffness interpolation (1), U is the global displacement vector, F<sup>ext</sup> is the global external force vector, and  $N_a$  is the total number of elements in the discretized finite element mesh. Note that, simultaneous inclusion of  $N_a$  nonlinear stress constraints evaluated at the center of the  $N_a$  elements increases the complexity of the optimization problem (10). To efficiently handle many local constraints, this study adopts an Augmented Lagrangian [60,61] (AL) based formulation with appropriate scaling [30]. Many studies [30,31,33,34,62-68] have used the AL approach to solve stressconstrained topology optimization problems over approximate aggregation methods like the p-norm [69], as the AL method preserves the local nature of stress and avoids the risk of stress constraints not being satisfied everywhere [31]. The AL formulation for the optimization problem (10), along with associated gradient expressions, are given in Appendix B. Note that, because voxel-based mesh is used in the optimization process, jagged boundary representation in the mesh would cause stress estimation error. To address this issue, a finite element check can be performed for the final optimized design with body-fitted mesh before fabrication [68]. The optimization formulation is implemented in Matlab, and requires ~ 14 hours with 1350 optimization iterations (each with 5 inner iterations for the AL unconstrained sub-problem) in a 64 GB RAM Intel(R) Xeon(R) Silver 4116 CPU @ 2.10 GHz processor.

#### 2.2. Fabrication of optimized designs

The optimization formulation (10) is combined with process-indu ced anisotropy from material extrusion 3D printing to fabricate stiff, strong, and lightweight structures with anisotropic and isotropic material phases. This subsection presents the adopted fabrication strategy for anisotropic and isotropic parts together with their interfaces in the optimized designs.

#### 2.2.1. Anisotropic and isotropic parts

Material extrusion 3D printing is used to generate both anisotropic and isotropic material phases by controlling the direction of the line type infill, i.e., print path inside the parts. For an anisotropic material phase, a single infill direction is assigned for all layers to realize the longitudinal direction, i.e., the direction with high stiffness and strength. For isotropic material phase, direction-independent stiffness and strength are approximately realized by using the line type infill orientated in the same direction for a single layer, but gradually changing from -90° to 90° in 30° increments at consecutive infill layers as the layer height increases. Fig. 1(a) shows the fabrication setup for anisotropic and isotropic infill patterns, and Fig. 1(b) shows the forcedisplacement responses of four uniaxial tension specimens printed in different orientations with same isotropic infill. The force-displacement curves indicate that the stiffness (represented by the slopes) and the strength (represented by the peak forces) remain almost the same for different orientations of adopted isotropic infill with respect to applied stress direction. The 30° increment works sufficiently well for this study with 1.2% and 3.2% deviations from mean values in  $E_{\rm iso}$ and  $\sigma_{iso}$ , respectively. A larger increment, such as 45°, gives larger deviations ( $\sim 6.8\%$  and  $\sim 5.9\%$  deviations from mean values in  $E_{\rm iso}$ and  $\sigma_{iso}$ , respectively). In the case where printed material has very high anisotropy, a smaller increment may be necessary to imitate better the isotropic behavior for printed parts. A suitable increment value may be decided by ensuring that the deviations from mean values in  $E_{\rm iso}$  and

**Table 1**Print parameters for additive manufacturing.

Parameter	Value
Filament diameter	1.75 mm
Nozzle diameter	0.4 mm
Layer height	0.2 mm
Line width	0.48 mm
Wall line count	1
Top/bottom layer count	2
Infill density	60%
Nozzle temperature	260 °C
Build plate temperature	115 °C
Print speed	40 m/s
Fan speed (first 10 layers)	0%
Fan speed (after 10 layers)	5%
Build plate adhesion	Brim
Heat retention	Skirt
Specimen thickness	6.8 mm

 Table 2

 Longitudinal stiffness and strength of anisotropic infill densities.

	0	1		
Infill density	Elastic modulus	0.2% yield strength	$E_{11}/\gamma$	$X_t/\gamma$
γ	$E_{11}$ (MPa)	$X_t$ (MPa)	(MPa)	(MPa)
100%	3004.67	36.04	3004.67	36.04
80%	2514.34	30.35	3142.93	37.94
60%	1888.22	23.39	3147.03	38.98

 $\sigma_{\rm iso}$  for different loading and infill directions are within an acceptable upper bound.

The open-source slicing software Ultimaker Cura 5.1.1 is used to assign infill directions and generate G-codes for the anisotropic and isotropic parts, which are then printed using Original Prusa i3 MK3S 3D printer and 3DxTech CarbonX ABS+CF (ABS with carbon fiber) filament. Some relevant print parameters are listed in Table 1.

We note that this study uses 60% infill density for anisotropic and isotropic parts, which implies that the material amount used to print the infill is  $\sim 60\%$  of the total available infill space. The adopted infill density allows relatively stronger interface fabrication for the optimized structures, as discussed in Section 2.2.2, without compromising the stiffness- and strength-to-mass ratios of the printed parts [70,71]. The uniaxial test results in Table 2 indicate that the adopted 60% infill density has slightly better stiffness and strength per unit infill density compared to 80% and 100% infill densities (along longitudinal direction for the anisotropic material phase) for the used ABS+CF material. However, infill densities lower than 60% are avoided as they risk unwanted premature failures due to large infill gaps and delamination. A higher number of wall lines and top/bottom layers are avoided to occupy larger cross-section areas with infill regions. Specimen out-ofplane thickness is adjusted considering various factors. While a thicker specimen is desired to avoid out-of-plane buckling and to increase the effective infill area in cross-section, an overly thick specimen may severely violate the plane stress assumption. In this study, specimen thickness is also restricted by the allowable gripping space between the test fixtures. Other listed print parameters in Table 1 are primarily related to ensuring acceptable print quality, and may need calibration for different print materials and 3D printers. Changing the print parameters can affect the relevant material properties (i.e., stiffness and strength parameters) as well as the anisotropy of the printed parts. In such cases, the optimized designs and force-displacement responses of the fabricated specimens are expected to vary from the results presented in this study.

#### 2.2.2. Interfaces

An important aspect of optimized structure fabrication is the realization of simulated interface behavior between different material phases. As the adopted numerical formulation does not specifically account for interface strength and stiffness, it inherently assumes that

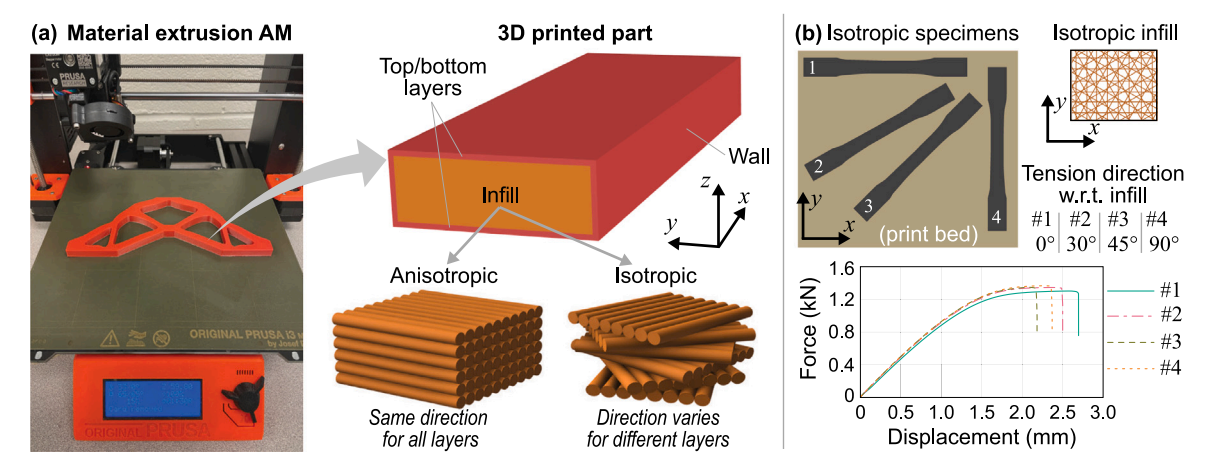


Fig. 1. Fabrication of anisotropic and isotropic parts; (a) assigned infill directions inside anisotropic and isotropic parts; (b) verification of direction-independent stiffness and strength for adopted isotropic infill printing.

any interface line is at least stronger than the weakest material phase connected to the interface. The numerical modeling is based on the assumption that the interface lines between two material phases are sufficient (i.e., stronger than at least the weakest neighboring material phase); thus, failure will occur in one of the neighboring material phases (instead of exactly at the interface line). Preliminary experimental investigations using a vertical interface (i.e., not s-shaped) showed that such an interface might fail before the neighboring material phases. Since this observation violates the assumption in the numerical framework, an s-shaped interface geometry (see Fig. 2(a)) is proposed for the material interfaces in the optimized designs to increase adhesion between the neighboring material phases and make the interface stronger than the connected material phases. The multiple joining material phases are 3D printed as a group (i.e., simultaneously) in a single attempt, without using any adhesive. This s-shaped interface fabrication not only makes the interface stronger, but also makes the interface region suitable for multi-axial load paths by enabling multiple infill orientations throughout the cross-section. The interface strength behavior is verified by uniaxial tension tests performed on specimens having different material phases. Fig. 2(b) presents 5 cases of interface tests, where material phase 1 is always fabricated with 0° infill direction, and material phase 2 is varied with different anisotropic (0°, 30°, 60°, 90°) and isotropic infills. For each case, three interface orientations are considered that are transverse, inclined, and longitudinal with the tension specimen. These three variations in interface orientations approximately represent the various possible interface orientations with respect to the load paths in the optimized designs. Fig. 2(b) indicates that this s-shaped interface has higher strength compared to all material phases for all three types of interface orientations, as the failure locations are observed outside interfaces for all test cases. The higher interface strength can be attributed to the horizontal adhesion of printed layers and high local infill density at the interface region compared to the adjacent members. The high local infill density also increases the stiffness of the interfaces. However, accounting for the increase in interface stiffness and strength in the optimization framework is beyond the scope of this study and can be an interesting future direction.

#### 2.3. Stiffness and strength characterization

Mechanical tests are performed for different anisotropic and isotropic phases to characterize their elasticity and strength parameters. As the topology optimization formulation uses linear elastic assumption, elasticity parameters are estimated from the initial, approximately linear part (within  $\approx 1\%$  strain) of the test responses. Strength parameters are obtained from the 0.2% offset yield strength estimates. Material

properties in tension and compression are obtained by following the methodologies in ASTM D635 and ASTM D695 standards, respectively. Shear properties are estimated using the same specimen geometry of the tension tests and following ASTM D3518 method, which recommends approximate shear response estimation from uniaxial tests of  $\pm 45^{\circ}$  laminates.

Fig. 3 summarizes the material characterization tests, including the specimen specifications, representative experimental data, and estimated average elasticity and strength parameters. The first two rows show the tension and compression test results for the anisotropic and isotropic phases, and the third row illustrates the adopted approach to estimate approximate shear parameters for the anisotropic phase. For each test case, 5 tests are performed using an INSTRON 68TM-30 universal loading machine to estimate average material parameters. The Poisson's ratios of anisotropic and isotropic material phases and the shear modulus of the anisotropic material phase are estimated by performing Digital image correlation (DIC) with the Ncorr (Matlab) software [72] and a SONY FE 2.8/24-70 GM II camera. Table 3 lists the final elasticity and strength parameter values adopted for topology optimization examples in Section 3. Notice that adopted elastic moduli for both anisotropic and isotropic material phases and von Mises strength for isotropic material phases are taken as average values from tension and compression to adapt to the topology optimization framework presented in 2.1. Furthermore, 90% of the experimentally obtained strength parameters are adopted for optimization to compensate approximate stress estimation error from FEA discretization, design post-processing from jagged to smooth boundaries, and various fabrication uncertainties.

#### 3. Results and discussions

This section presents the advantages of the proposed methodology in additive manufacturing of lightweight, stiff, and strong structures with design optimization, fabrication, and experimental investigations. The first example shows structural strength enhancement with anisotropic stress constraints; the second example illustrates the advantages of using optimized infill orientations and s-shaped interfaces in optimized design fabrication; and the third example demonstrates the effect of considering tension–compression strength asymmetry on design optimization and failure behavior. The examples with design optimizations predict satisfaction or violation for Tsai–Wu and von Mises yield criteria corresponding to candidate anisotropic and isotropic material phases, respectively, with the yield function measure (YFM) fringe plots. This yield function measure is calculated as YFM =  $\left[\varepsilon + (1-\varepsilon)\bar{\rho}_{\varepsilon}(\rho)^{p_{\rho}}\right]f_{\varepsilon}^{(\xi)}(\xi^{(1)},\dots,\xi^{(N_{\varepsilon})},\mathbf{U})$ , and performs similarly as a normalized stress measure with YFM > 1 indicating yield criterion

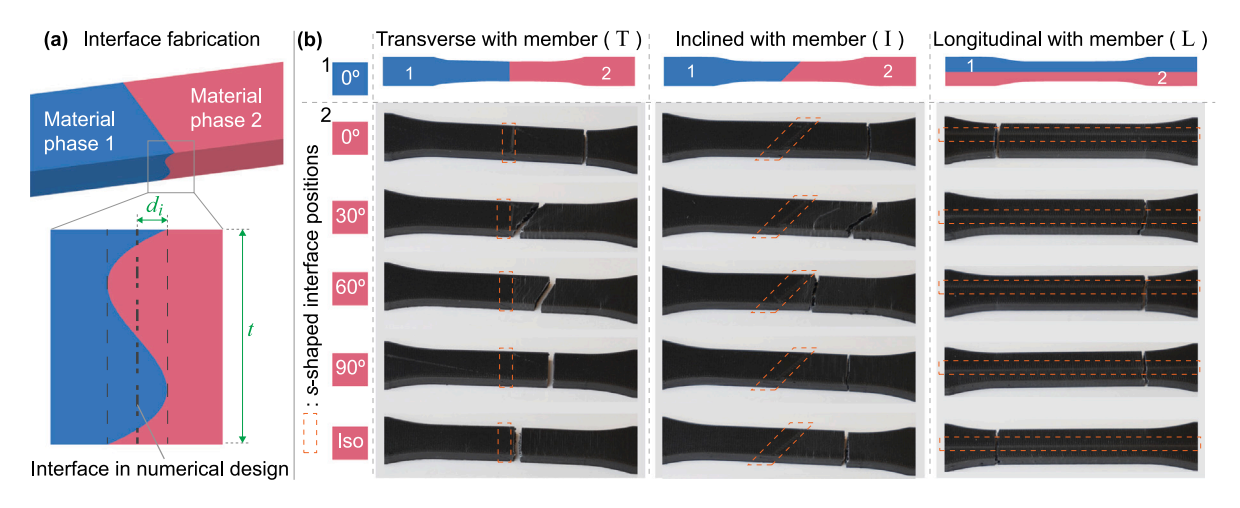


Fig. 2. Interface fabrication and strength tests; (a) s-shaped interface geometry,  $d_i = 4.0$  mm, t = 6.8 mm; (b) uniaxial tension test results showing failures outside the different interface orientations for different adjacent material phases.

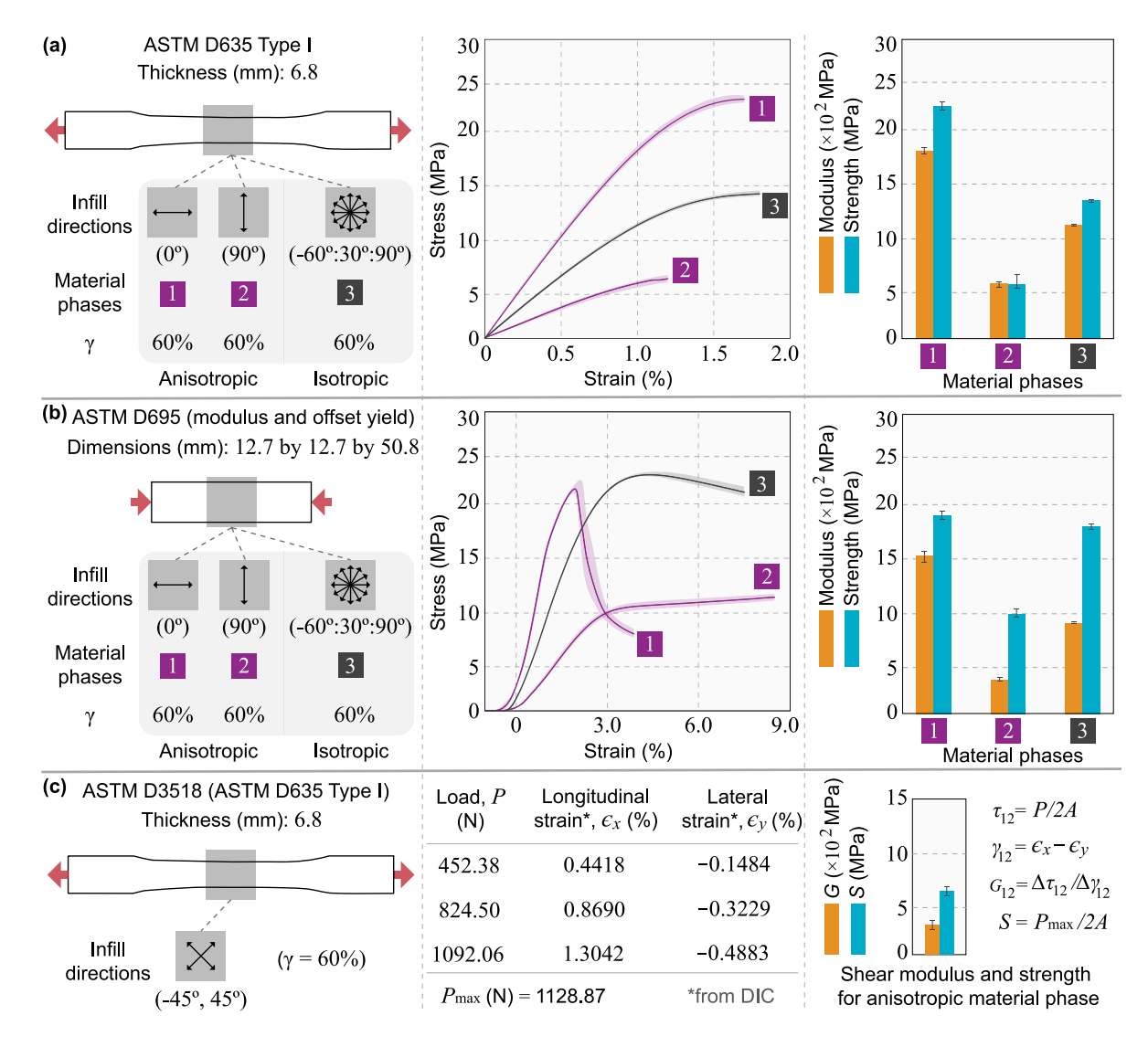


Fig. 3. Characterized stiffness and strength parameters for anisotropic and isotropic material phases; (a) specimen details, average stress-strain curves and parameter values for tension, (b) specimen details, average stress-strain curves and parameter values for compression, (c) specimen details, related calculations from test data, and average parameter values for shear.

**Table 3**Experimentally estimated stiffness and strength parameters.

Material phases	Parameters	Estimates for tension (MPa)	Estimates for compression (MPa)	Estimates for shear (MPa)	Values adopted for topology optimization <sup>a</sup>
	$E_{11}$	1888.22 ± 79.2	1595.36 ± 118.05	-	1741.79
	$E_{22}$	$556.82 \pm 67.06$	$341.48 \pm 44.77$	-	449.15
	$\nu_{12}$	$0.23 \pm 0.03$	-	-	0.23
Anisotropic( $\gamma = 60\%$ )	$G_{12}$	_	-	$300.86 \pm 48.92$	300.86
	$X_t$	$23.39 \pm 0.9$	-	-	21.05
	$Y_t$	$5.490 \pm 1.55$	-	-	4.94
	$X_c$	_	$20.01 \pm 0.87$	-	18.01
	$Y_c$	_	$10.02 \pm 0.90$	-	9.02
	S	-	-	$6.54 \pm 0.48$	5.89
Isotropic( $\gamma = 60\%$ )	$E_{\rm iso}$	1143.28 ± 25.74	912.13 ± 14.55	-	1027.71
	$v_{ m iso}$	$0.36 \pm 0.03$	-	-	0.36
	$ar{\sigma}_{ m iso}$	$13.94 \pm 0.35$	$18.89 \pm 0.61$	-	14.77

<sup>&</sup>lt;sup>a</sup>90% of experimentally obtained strength parameters are used for topology optimization.

violation. While this study considers six or eight candidate anisotropic orientations for the demonstrated examples, a different number of candidate orientations may be considered for design problems with different dimensions, material properties, and fabrication methodologies. In general, very few candidate orientations may reduce the performance improvement, whereas too many candidate orientations may lead to increased computational cost and many closely-spaced interface regions.

#### 3.1. Example 1: structural strength enhancement

This example compares two design cases to demonstrate the increase in structural strength with anisotropic stress-constrained topology optimization. The first case minimizes the objective function in (10) (i.e., the weighted sum of normalized mass and compliance) without considering the stress constraints, while the second case minimizes the same objective with stress constraints. Both cases include anisotropic and isotropic material phases with infill density  $\gamma=60\%$ , and a compliance weight factor w=0.35. Fig. 4(a) shows the design domain and candidate material phases, with six pre-selected infill orientations for the anisotropic material phase. Fig. 4(b) discusses the optimized designs along with their YFM fringe plots and principal stress states with yield surface contours [45]. Fig. 4(c) presents an example of a partially complete fabricated design to illustrate printed infill directions inside the specimen and s-shaped interfaces.

For the design optimized without stress constraints, several locations (especially two sharp corners) in the design have YFM values exceeding 1 and principal stress states outside the yield surface contours, both indicating premature failure of the structure by local stress state exceeding material strength. In contrast, the design optimized with stress constraints restricts the maximum YFM value to 1, i.e., restricts the principal stresses to be inside the yield surface contour throughout the design. In presence of stress constraints, the optimizer marginally increases the compliance and material usage to partially remove the sharp corners and avoids stress concentration beyond material strength. Notice that, for both design cases, the optimizer chooses the infill orientations closest to the directions of principal stress paths at any location to increase structural stiffness while minimizing volume. This process implicitly also increases the structural strength, i.e., load carrying capacity, as infills oriented along stress paths usually provide most strength. However, the second design case with stress constraints increases the structural strength both implicitly by aligning infills along stress paths, and also explicitly by suitable changes in structural geometry.

The optimized designs obtained from the two design cases are fabricated and tested to validate the predicted enhanced structural strength with anisotropic stress-constrained topology optimization. Fig. 5(a) shows the test setup, tested specimens corresponding to the two design cases, and their load–displacement histories. The roller boundary

condition in design domain (see Fig. 4(a)) is realized using a 20 mm thick PLA-printed fixture having 100% infill density. The fabricated specimens are loaded till failure with a 1.5 mm/min displacement rate. The experimentally observed trend in stiffness and strength performances of the two structures are consistent with the predicted numerical results from Fig. 4(b). The load-displacement plot shows that the specimen optimized with stress constraints attains a higher peak load before failure and similar structural stiffness (i.e., slope of the load-displacement curve) compared to the specimen optimized without stress constraints. Fig. 5(b) compares the predicted failure locations (with YFM fringe plots) for the optimized designs from Fig. 4(b) and the observed failure locations in the tested specimens. For the design case without stress constraints, stress concentration with YFM exceeding 1 is observed near the sharp corners, the supports, and at some member interfaces. The corresponding fabricated specimen fails from one of the sharp corners, which indicates a close match with predicted failure. For the design case with stress constraints, some stress concentration is predicted near the partially removed sharp corners, supports, and some member interfaces. However, comparatively lower YFM values ( $\approx 1$ ) at those stress concentration regions results in a higher failure load for the corresponding fabricated specimen. In this case, the fabricated design uses a slightly more material amount and different topology to enhance the peak load-to-mass ratio by 9%.

Note that, the fabricated s-shaped interfaces have multi-axial infills and higher infill densities than the interfaces in the numerical model. As a result, the tested specimen for the stress-constrained case does not fail at the interface as predicted. The prediction can be more accurate by exclusively modeling accurate stiffness and strength properties for the interface regions. However, exclusive modeling of s-shaped interfaces may increase the complexity of the optimization framework and can be an interesting direction for future work. In this study, the adopted fabrication approach further enhances the strength of printed structures by strengthening the joints, which are often the weakest parts in structures optimized for high stiffness using unidirectionally stiff and strong anisotropic material phases.

#### 3.2. Example 2: stiff, strong, and lightweight fabrication

This example illustrates the advantages of optimized infill and s-shaped interface fabrication in material extrusion-based additive manufacturing of stiff, strong, and lightweight structures. The topology (i.e., structural geometry) of the design optimized with stress constraints from previous example is used with different infill generation methods commonly used in material extrusion 3D printing to fabricate different test structures. These test structures do not involve any infill optimization and s-shaped interfaces. Fig. 6 compares the structural stiffness (i.e., slope of load–displacement curve), strength (i.e., peak load), and material used (i.e., mass) of the fabricated test structures with the design having optimized infill and s-shaped interfaces. The

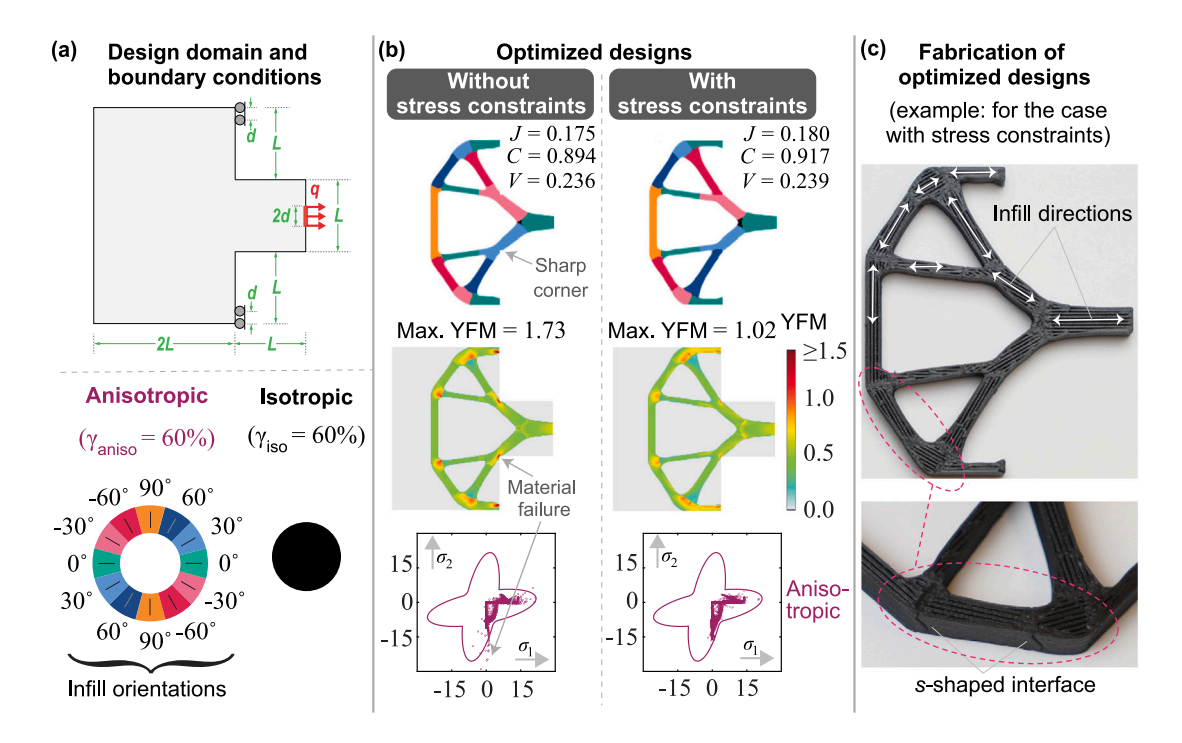


Fig. 4. Local failure prevention with anisotropic stress constraints; (a) design domain and boundary conditions (BCs), L = 60 mm, d = 6 mm, q = 15 kN/mm, and candidate material phases; (b) comparison of designs optimized without and with anisotropic strength; (c) printed infill directions and s-shaped interfaces for an optimized design fabrication.

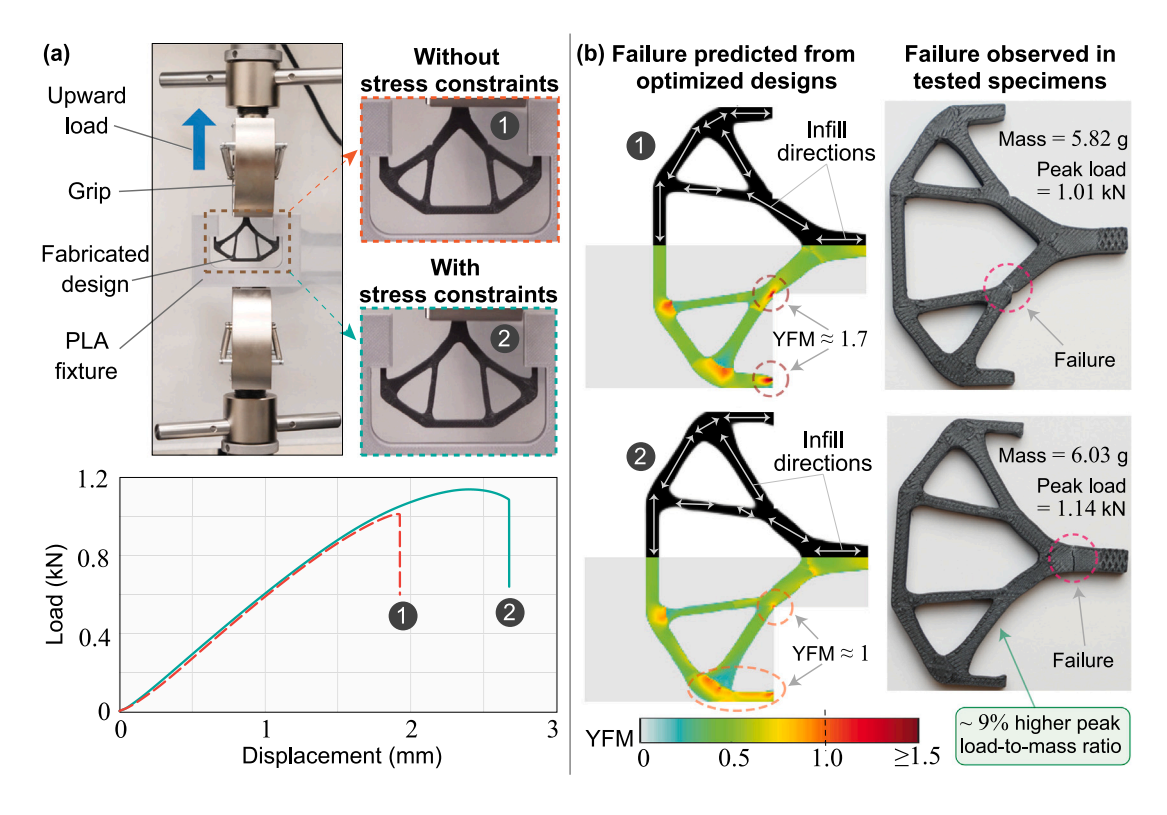


Fig. 5. Experimental evaluation of optimized designs in Example 1; (a) test setup and load-displacement responses; (b) comparison of numerically predicted and experimentally observed failures.

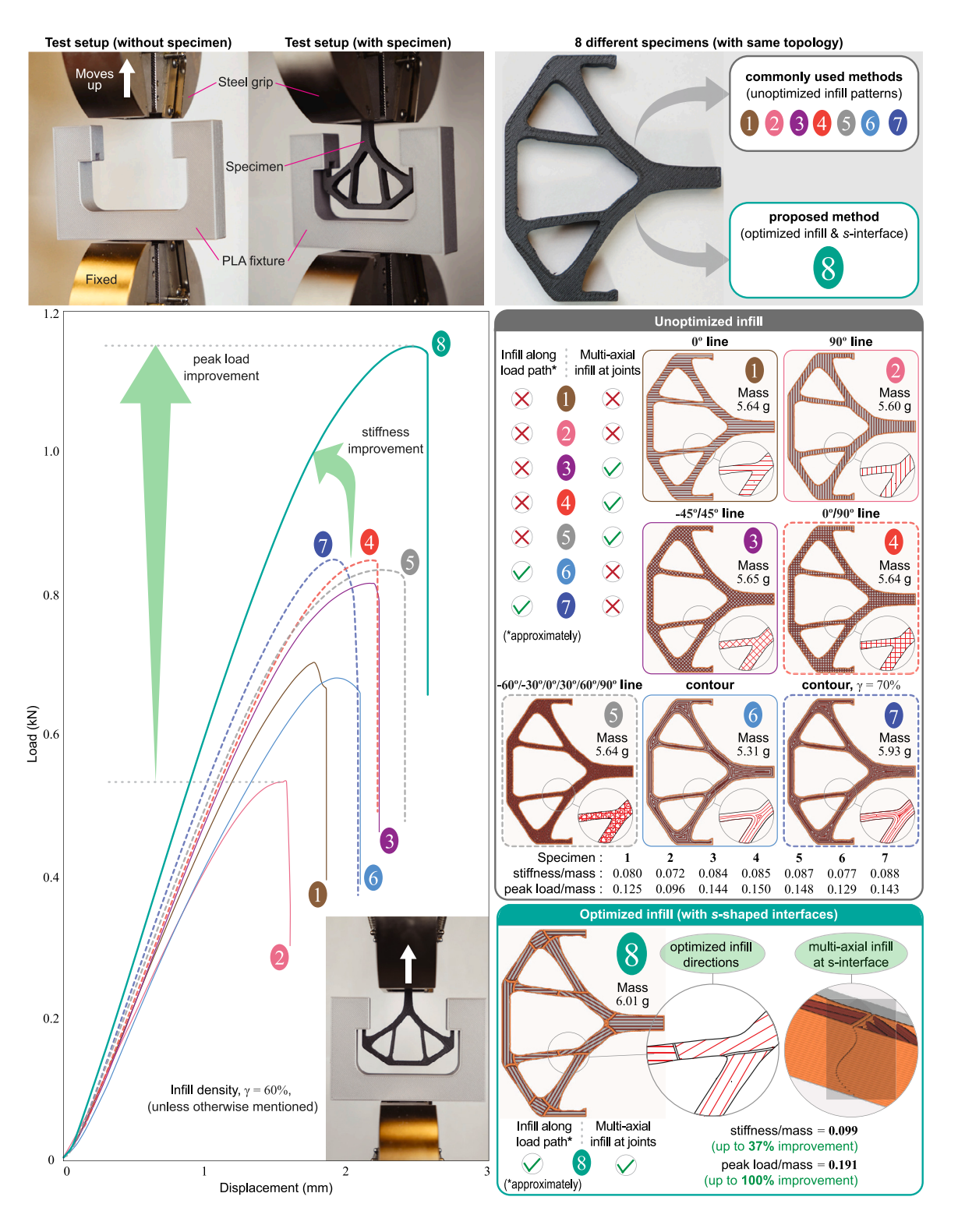


Fig. 6. Mechanical performances of designs with same topology and different infill patterns. The adopted fabrication strategy with optimized infill and s-shaped interface shows superior structural stiffness- and strength-to-mass ratios compared to common infill fabrication methods. Experimental validation of un-optimized infill (cases 1–7) versus optimized infill (case 8). Compared to common infill fabrication methods, using the proposed optimal infill and s-interface (case 8) lead to up to 37.19% and 100.51% improvement in stiffness- and strength-to-mass ratios, respectively, of the 3D printed structure. The stiffness is defined as the initial slope of the FD curve, and the strength of the structure is defined as the peak load in the FD curve. Units: kN/mm-g for stiffness/mass, and kN/g for peak load/mass.

load–displacement plot shows the superior overall structural stiffness and strength resulting from the proposed optimization and fabrication method. Note that, the optimized-infill structure uses more amount of material because of the adopted s-shaped interface fabrication, as the infill densities ( $\gamma$ ) near such interfaces becomes higher than 60%. Despite using more material, the optimized-infill structure obtains higher stiffness- and peak load-to-mass ratios, indicating efficient material usage.

The high stiffness and strength performance per unit mass is mostly attributed to infill orientations aligned with load paths in the structure. In this example, the load paths are mostly uniaxial in slender members and multi-axial in joints, i.e., at the intersection of multiple members, and they are oriented approximately along the member lengths. Among test cases 1 and 2, the former has more members with infill oriented along load paths and therefore achieves a higher stiffness- and peak load-to-mass ratio. Test cases 3, 4, and 5 have higher stiffness- and peak load-to-mass ratio compared to test cases 1 and 2, as the latter ones have uniaxial infill in the joints with multi-axial load paths. Test cases 3, 4, and 5 show similar stiffness- and load-to-mass ratio as all of these structure has some part of their multi-axial infill orientated along the load paths in all members. Test case 6 with contour infill has lower stiffness- and peak load-to-mass ratio despite having infills aligned with load paths in the members. The probable reason is the voids at the joints, which significantly decrease the overall stiffness and strength of the structure. Test case 7 with the same contour infill and a higher infill density ( $\gamma = 70\%$ ) fills most of the voids at the joints and therefore shows stiffness- and peak load-to-mass ratios comparable to test cases 3, 4, and 5. Test case 8 with optimized infill has infill directions in slender members mostly along load paths similar to test case 7, and therefore a similar stiffness and strength performance is expected. However, the s shape of the interfaces in test case 8 allows infills of both intersecting members to be present at the interface regions that result in multi-axial infill patterns at the joints. Moreover, the local increase in infill density near interfaces also increases the stiffness and strength of the joints. Therefore, test case 8 with optimized infill and s-shaped interface with the proposed methodology achieves a higher stiffness- and strength-to-mass ratio compared to other common infill generation methods for a topology optimized structure. Note that the proposed methodology does not require extensive load path calculation and infill programming at each location according to the stress magnitude. Instead, it bypasses the infill overlapping problem by suitable topology changes near stress concentrations and reduces the post-processing complexity for fabrication after design optimization.

#### 3.3. Example 3: tension-compression strength asymmetry

This example demonstrates that the proposed methodology takes into account the tension-compression strength asymmetry of anisotropic printed parts, particularly in regions with multi-axial load paths. Two design cases are considered for comparison. The first design case Dsg. TW uses appropriate Tsai-Wu and von Mises criteria for anisotropic and isotropic material phases from Table 3, whereas the second design case Dsg. VM assumes the uniaxial longitudinal tensile strength of the anisotropic infill as a von Mises stress limit for all candidate material phases (i.e.,  $\sigma_{lim} = X_t$ ). Both design cases are optimized separately for two loading scenarios in tension and compression with the same design domain, boundary conditions, and candidate anisotropic and isotropic material phases as shown in Fig. 7(a). Fig. 7(b) presents the optimized designs for Dsg. TW and Dsg. VM for tension and compression loading, along with their yield function measure (YFM) fringe plots. For the case Dsg. VM, the YFM plots evaluated with actual Tsai-Wu strength parameters are also included for comparison. A compliance weight factor of w = 0.3 is used for all design cases in this example.

The design case Dsg. TW obtains two different optimized designs for tension and compression loading. For tension loading, the critical regions, i.e., regions with YFM  $\approx$  1, are the boundary members in

compression (i.e., boundary members which are not adjacent to the re-entrant corner in the design domain). For compression loading, the critical region shifts to the two boundary members adjacent to the re-entrant corner as they experience a compression stress state under compression loading. As the uniaxial strength (along infill or longitudinal direction) of the used anisotropic material phase is higher in tension compared to compression, the different members become critical for tension and compression loading according to their tension or compression stress states. In contrast, Dsg. VM design case results in the same optimized design and YFM plots for both tension and compression loading while using von Mises yield criterion, which considers equal strength in tension and compression. In both tension and compression loading, the re-entrant corner is identified as critical with maximum YFM ≈ 1. However, the same design Dsg. VM evaluated with Tsai-Wu criterion shows maximum YFM  $\approx$  1.5, indicating overestimation of material strength in Dsg. VM. Furthermore, the member interfaces and the boundary members adjacent to the re-entrant corner are also identified with high YFM for tension and compression loading, respectively, in addition to the re-entrant corner. Notice that, all optimized designs prefer an isotropic material phase near the re-entrant corner, as this region has multiple load paths from many intersecting members. For all the slender members with mostly unidirectional stress paths, the optimizer prefers anisotropic material phases to increase the stiffnessand strength-to-mass ratios of the optimized designs.

The optimized designs from Dsg. TW and Dsg. VM are fabricated and tested to compare their relative load-carrying performances and failure locations. Fig. 8(a) shows the test setup and load-displacement responses for tension and compression loadings on the fabricated specimens. For tension loading, both Dsg. TW and Dsg. VM specimens have near-equal structural stiffness and peak loads. However, the failure mechanisms for the two specimens are different and reflect the effect of using different strength criteria in topology optimization. The Dsg. TW specimen fails due to in-plane buckling of a member in nearly uniaxial compression, whereas the Dsg. VM specimen fails due to sharp crack propagation from a re-entrant corner which is in multi-axial tension. For compression loading, both Dsg. VM and Dsg. TW has similar failure mechanisms, whereas the latter achieves a higher peak load.

For the tested specimens, the failure behaviors can be related to the adopted yield criteria for optimization and the corresponding optimized design topology. For tension loading, the re-entrant corner experiencing multi-axial tension is replaced by a smooth round-shaped geometry for Dsg. TW as the Tsai-Wu criterion assumes lesser strength in multi-axial tension compared to uniaxial tension. The Dsg. VM design retains the re-entrant corner as it overestimates the multi-axial tension strength using a von Mises criterion. As a result, the Dsg. VM fails from a sharp crack at the re-entrant corner during the experiment. While Dsg. TW fails at the same load level due to the buckling of a compression member, no crack appears at the re-entrant corner location. Since the buckling is not considered in the formulation, it is not predicted by the simulation. The incorporation of buckling is important and will be investigated in the future study. For compression loading, Dsg. TW and Dsg. VM retains the re-entrant corner partially and completely, respectively, as the predicted strength in multi-axial compression can be higher than uniaxial compression for both Tsai-Wu and von Mises yield criteria. Both specimens fail at the compression member adjacent to the re-entrant corner, while Dsg. VM achieves ~ 10.8% lower peak load as it overestimates the compression strength of the anisotropic material phase. Note that, failure regions are consistently predicted with high Tsai-Wu YFM values for all design cases.

#### 4. Conclusions

This study proposes and experimentally validates an AM-oriented topology optimization framework that incorporates anisotropic properties in strength and stiffness induced by the material extrusion additive manufacturing process. These anisotropic material properties are

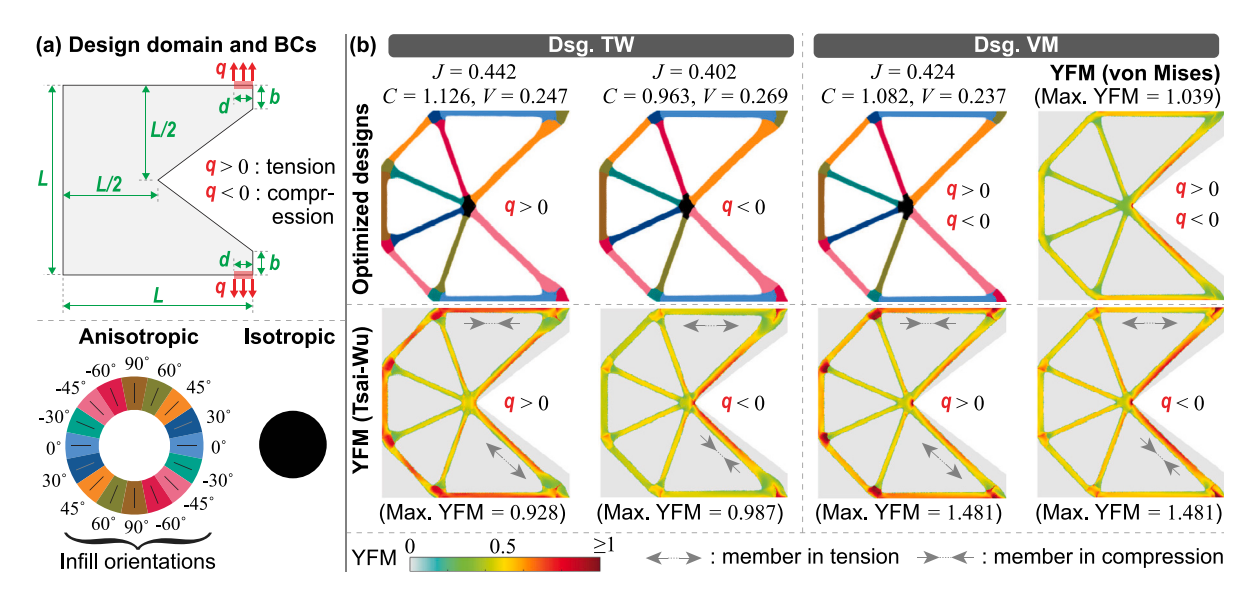


Fig. 7. Topology optimization with tension and compression loading for asymmetric tension-compression strength; (a) design domain and boundary conditions (BCs), L = 160 mm, d = 12 mm, b = 20 mm, q = 4.17 kN/mm, and candidate material phases; (b) comparison of strength-based topology optimization for tension and compression loading considering anisotropic Tsai-Wu (Dsg. TW) and isotropic von Mises (Dsg. VM) criteria.

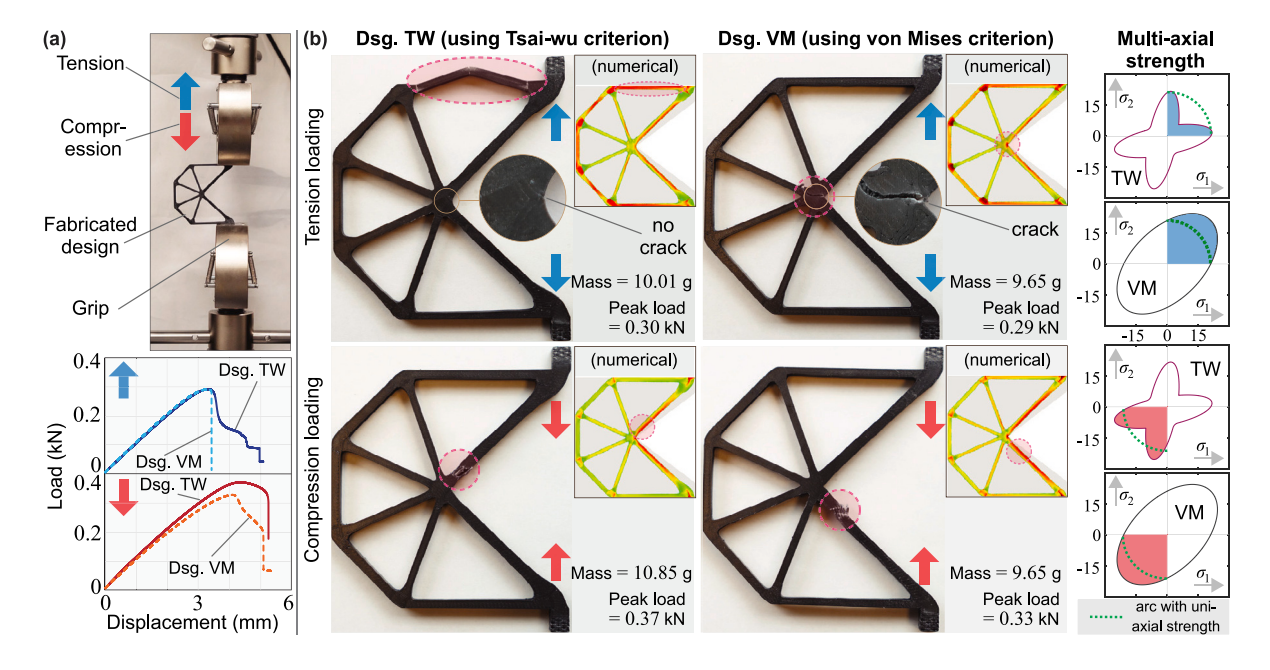


Fig. 8. Experimental evaluation of optimized designs in Example 2; (a) test setup and load–displacement responses for tension and compression loading; (b) comparison of numerically predicted and experimentally observed failures.

leveraged to design stiff, strong, and lightweight structures by simultaneously optimizing the design geometry and the orientation of in-plane infill directions. Anisotropic and isotropic material phases are fabricated by controlling the print path or infill direction within the printed parts. An effective interface fabrication method is adopted to satisfy the assumptions in the numerical simulation regarding the relative strengths of the interface and adjacent material phases. The stiffness and strength parameters for the anisotropic and isotropic material phases are obtained from material characterization tests. Several numerical and experimental investigations demonstrate the effectiveness of the proposed design optimization and fabrication methodology.

The experimental results from the fabricated and tested optimized designs agree with the predicted stiffness and strength performance from numerical simulations. Both numerical optimization and experimental tests demonstrate that incorporating anisotropic strength in the optimization formulation increases overall structural strength, i.e., load-carrying capacity, with only a nominal increase in material usage. The stress constraints help to reduce stress concentration beyond the material strength limit in the design with suitable changes in structural topology. In addition to the topology change, two other key factors contributing to higher stiffness- and strength-to-mass ratios are identified as infill alignment along the load paths and multi-axial dense

infill at the member joints. The numerical results identify potential failure-prone regions due to high stress concentration and asymmetric tension—compression strength of printed parts, which are mostly consistent with the experimental observations. The experimental results from the fabricated designs demonstrate the capability of the methodology in utilizing process-induced anisotropy to generate stiff, strong, and lightweight designs.

The proposed methodology can be improved by accounting for in-plane buckling and tension-compression asymmetry in stiffness as well as including interface stiffness and strength to improve both the objective function value and failure prediction. While this study focuses on process-induced anisotropy in material extrusion printing, the proposed methodology can be adapted for other additive manufacturing technologies with process-induced anisotropy by appropriate characterization of direction-dependent stiffness and strength of printed material, and suitable fabrication innovation (such as modular fabrication with strong interfaces) to freely align stronger printed direction along optimized anisotropy/orthotropy orientations. The framework can also be adapted for fiber-reinforced and functionally graded topology optimized structures, where anisotropy is induced by fiber orientation and anisotropic microstructure geometry, respectively. However, unless interface strength is explicitly considered in the optimization framework, necessary physical or chemical adjustments should be incorporated in the fabrication process to make the interfaces stronger than the weakest connected material phase. Furthermore, more accurate functions can be used as yield functions, with appropriate adjustments (e.g., smoothening of sharp corners in the yield surface) to represent failure in the candidate anisotropic and isotropic material phases. Although the examples presented here are for 2D plane stress designs, the adopted topology optimization framework is general and can be extended to 3D design problems. Therefore, fabricating and experimentally investigating optimized complex 3D structures are also promising research directions.

#### CRediT authorship contribution statement

Rahul Dev Kundu: Writing – review & editing, Writing – original draft, Visualization, Validation, Software, Methodology, Investigation, Formal analysis. Xiaojia Shelly Zhang: Writing – review & editing, Writing – original draft, Supervision, Resources, Project administration, Methodology, Investigation, Funding acquisition, Formal analysis, Conceptualization.

#### Declaration of competing interest

The authors declare that they have no known competing financial interests or personal relationships that could have appeared to influence the work reported in this paper.

#### Data availability

Data will be made available on request.

#### Acknowledgments

The authors would like to acknowledge the following financial supports. X.S. Zhang and R.D. Kundu were supported by the U.S. National Science Foundation (NSF) EAGER Award CMMI-2127134 and CAREER Award, United States CMMI-2047692. The information provided in this paper is the sole opinion of the authors and does not necessarily reflect the view of the sponsoring agencies.

#### Appendix A. Filter, projection, and tailored HSP mapping

Most topology optimization studies use filter [50] and projection [51]to achieve mesh-independent and discrete designs [50,53]. The filtered variables [48,49] are obtained from the design variables as

$$\tilde{\rho}_{e} = \frac{\sum_{j \in n_{e}(R_{\rho})} w\left(\mathbf{x}_{j}\right) v_{j} \rho_{j}}{\sum_{j \in n_{e}(R_{\rho})} w\left(\mathbf{x}_{j}\right) v_{j}} \quad \text{and}$$

$$\tilde{\xi}_{e}^{(k)} = \frac{\sum_{j \in n_{e}(R_{\xi})} w\left(\mathbf{x}_{j}\right) v_{j} \xi_{j}^{(k)}}{\sum_{j \in n_{e}(R_{\xi})} w\left(\mathbf{x}_{j}\right) v_{j}}, \quad k = 1, \dots, N_{\xi},$$
(A.1)

where  $\mathbf{x}_j$  and  $v_j$  are the centroid and the volume of element j, respectively,  $\mathbf{n}_{\rm e}$  is the neighborhood of element e defined by a filter radius R, i.e.,  $\mathbf{n}_{\rm e}(R) = \left\{j: \left\|\mathbf{x}_j - \mathbf{x}_e\right\|_2 \leq R\right\}, w\left(\mathbf{x}_j\right)$  is the cubic weight function defined as  $w\left(\mathbf{x}_j\right) = \max(0, 1 - \left\|\mathbf{x}_j - \mathbf{x}_e\right\|_2 / R)^3$ , and  $R_\rho$  and  $R_\xi$  are the filter radii for density and material design variables, respectively. The filtered variables undergo the smoothed Heaviside projection [51,56] to output the Heaviside projected variables as

$$\begin{split} \bar{\rho}_e &= \frac{\tanh(\beta_\rho \eta_\rho) + \tanh(\beta_\rho (\tilde{\rho_e} - \eta_\rho))}{\tanh(\beta_\rho \eta_\rho) + \tanh(\beta_\rho (1 - \eta_\rho))} \quad \text{and} \\ \bar{\xi}_e^{(k)} &= \frac{\tanh(\beta_\xi \eta_\xi) + \tanh(\beta_\xi (\tilde{\xi}_e^{(k)} - \eta_\xi))}{\tanh(\beta_\xi \eta_\xi) + \tanh(\beta_\xi (1 - \eta_\xi))}, \quad k = 1, \dots, N_\xi, \end{split} \tag{A.2} \end{split}$$

where the projection discreteness is regulated by the Heaviside parameters  $\beta_o$  and  $\beta_{\varepsilon}$ , and the projection thresholds  $\eta_o$  and  $\eta_{\varepsilon}$ .

The material filtered and Heaviside projected variables further undergo a tailored HSP mapping to satisfy the condition  $\sum_{i=1}^{N_m} (\bar{m}_e^{(i)}) = 1$  for a physical structure, as each physical material variable  $\bar{m}_e^{(i)}$  represents the portion of  $i^{\text{th}}$  candidate material phase in an element e in this study. To satisfy the equality condition, original HSP scheme [52] is applied to obtain the first  $(N_m-1)$  physical material variables, and their values are used to obtain the last physical material variable. This tailored HSP scheme obtains  $N_m$  physical material variables from  $N_\xi = (N_m-1)$  material Heaviside projected variables as

$$\begin{split} \bar{m}_e^{(i)} &= \sum_{j=1}^{2^{(N_m-1)}} b_j^{(i)} \left( (-1)^{(N_m-1+\sum_{i=1}^{N_m-1} c_j^{(k)})} \prod_{k=1}^{(N_m-1)} (\bar{\xi}_e^{(k)} + c_j^{(k)} - 1) \right), \\ i &= 1, \dots, N_m - 1, \\ \text{and,} \quad \bar{m}_e^{(N_m)} &= 1 - \sum_{i=1}^{N_m-1} (\bar{m}_e^{(i)}) \end{split} \tag{A.3}$$

where,  $c_j^{(i)}=\{0,1\}$  is the  $j^{\rm th}$  vertex of  $(N_m-1)$ -dimensional unit hypercube for the  $i^{\rm th}$  candidate material, and  $b_j^{(i)}$  is the mapped vertex of  $(N_m-1)$ -dimensional standard simplex domain calculated as

$$b_j^{(i)} = \begin{cases} \frac{c_j^{(i)}}{\sum_{i=1}^{N_m - 1} c_j^{(i)}}, & \text{if } \sum_{i=1}^{N_m - 1} c_j^{(i)} \ge 1\\ 0, & \text{otherwise.} \end{cases}$$
 (A.4)

The filtering with Heaviside projection strategy, together with SIMP-based stiffness penalization scheme, helps to reduce material mixing at the end of optimization. Material mixing amounts estimated using  $M_m^{(i)} = \frac{1}{N_e} \sum_{e=1}^{N_e} 4m_e^{(i)} (1-m_e^{(i)}) \times 100\%, \ i=1,\dots,N_m, \ [50,56]$  are restricted to 7% for each of the ith material phase in the design examples. Furthermore, most of the multi-material phase mixing occur at interfaces, and we adopt s-shaped interface fabrication which allows infill mixing throughout cross-section within the interface area.

## Appendix B. Augmented-Lagrangian formulation and corresponding sensitivity calculations

In the adopted Augmented-Lagrangian formulation, the local stress constraints are augmented to the original objective function from (10)

(B.1)

using Lagrangian parameter estimators and a penalty term to formulate an unconstrained optimization sub-problem, which is solved sequentially to approximate the solution of the original constrained problem. The unconstrained optimization sub-problem at the nth optimization step is given by [30]

$$\begin{split} \min_{\rho',\xi'^{(1)},...,\xi'^{(N_{\xi})}} \psi'^{(n)} \left( \rho',\xi'^{(1)},...,\xi'^{(N_{\xi})} \right) &= J \left( \rho',\xi'^{(1)},...,\xi'^{(N_{\xi})} \right) + \\ &\frac{1}{N_{e}} \sum_{e=1}^{N_{e}} \left( \lambda_{e}^{(n)} h_{e}^{(n)} \left( \rho',\xi'^{(1)},...,\xi'^{(N_{\xi})} \right) \right) \\ &+ \frac{\mu^{(n)}}{2} h_{e}^{(n)} \left( \rho',\xi'^{(1)},...,\xi'^{(N_{\xi})} \right)^{2} \right), \end{split}$$

where  $\psi^{(n)}\left(\rho',\xi'^{(1)},\ldots,\xi'^{(N_{\xi})}\right)$  is the nth step (augmented) objective function with  $\rho'$  and  $\xi'^{(1)},\ldots,\xi'^{(N_{\xi})}$  denoting dummy design variables corresponding to  $\rho$  and  $\xi^{(1)},\ldots,\xi^{(N_{\xi})}$ , and  $h_e\left(\rho',\xi'^{(1)},\ldots,\xi'^{(N_{\xi})}\right)$  is the equality constraint for eth element given by

$$\begin{split} h_e^{(n)}\left(\rho', \xi'^{(1)}, \dots, \xi'^{(N_{\xi})}\right) &= \\ \max\left(g_e\left(\rho', \xi'^{(1)}, \dots, \xi'^{(N_{\xi})}, \mathbf{U}_l(\rho', \xi'^{(1)}, \dots, \xi'^{(N_{\xi})})\right), -\frac{\lambda_e^{(n)}}{\mu^{(n)}}\right), \end{split} \tag{B.2}$$

where  $\lambda_e^{(n)}$  is an estimate of the Lagrange multiplier estimator for eth element, and  $\mu^{(n)}$  is a penalty coefficient. The updated design variables for next sub-problem are the solution of the current sub-problem (B.1), i.e.,  $\rho^{(n+1)} = \rho'^*$  and  $\{\xi'^{(1)}, \dots, \xi'^{(N_{\xi})}\}^{(n+1)} = \{\xi'^{(1)}, \dots, \xi'^{(N_{\xi})}\}^*$ . The Lagrange multiplier estimators and the penalty coefficient for the next sub-problem are obtained from the updated design variables as

$$\begin{split} \mu^{(n+1)} &= \max \left( \alpha \mu^{(n)}, \mu^{(\max)} \right) \text{ and} \\ \lambda_e^{(n+1)} &= \lambda_e^{(n)} + \mu^{(n)} h_e^{(n)} \left( \rho^{(n+1)}, \{ \xi'^{(1)}, \dots, \xi'^{(N_\xi)} \}^{(n+1)} \right), \end{split} \tag{B.3}$$

where  $\alpha>1$  is a constant, and  $\mu^{(max)}$  is an upper bound for the penalty coefficient to avoid numerical instability. This study uses gradient-based Method of Moving Asymptotes (MMA) [73] to solve the unconstrained sub-problems. The gradient expressions with respect to the design variables are provided in following.

The sensitivity of the AL function with respect to  $\rho$  and  $\xi^{(i)}$ ,  $i=1,\ldots,N_{\xi}$  is obtained through the chain rule:

$$\frac{\partial \psi^{(n)}}{\partial \rho_e} = \sum_{i=1}^{N_e} \frac{\partial \psi^{(n)}}{\partial \bar{\rho}_j} \frac{\partial \bar{\rho}_j}{\partial \bar{\rho}_j} \frac{\partial \tilde{\rho}_j}{\partial \rho_e},\tag{B.4}$$

$$\frac{\partial \psi^{(n)}}{\partial \xi_e^{(k)}} = \sum_{j=1}^{N_e} \frac{\partial \psi^{(n)}}{\partial \bar{m}_j^{(i)}} \frac{\partial \bar{m}_j^{(i)}}{\partial \bar{\xi}_j^{(k)}} \frac{\partial \bar{\xi}_j^{(k)}}{\partial \xi_j^{(k)}} \frac{\partial \bar{\xi}_j^{(k)}}{\partial \xi_e^{(k)}}, \tag{B.5}$$

In Eqs. (B.4) and (B.5), the sensitivities of the physical variables with respect to design variables can be computed from (A.1), (A.2), and (A.3) (see [31,74]). The sensitivities of the AL objective function (B.1) with respect to the physical variables are derived as

$$\frac{\partial \psi^{(n)}}{\partial \bar{\rho}_{e}} = w \left( -\mathbf{U}^{T} \frac{\partial \mathbf{F}_{\text{int}}}{\partial \bar{\rho}_{e}} \right) + (1 - w) \frac{\sum_{i=1}^{N_{m}} \hat{\gamma}_{i} \bar{m}_{e}^{(i)} v_{e}}{\sum_{k=1}^{N} v_{k}} + \frac{1}{N} \left( \left[ \lambda_{e}^{(n)} + \mu^{(n)} h_{e}^{(n)} \right] \frac{\partial h_{e}^{(n)}}{\partial \bar{\rho}_{e}} + \mathbf{\Lambda}^{T} \frac{\partial \mathbf{F}_{\text{int}}}{\partial \bar{\rho}_{e}} \right) \tag{B.6}$$

$$\frac{\partial \psi^{(n)}}{\partial \bar{m}_e^{(i)}} = w \left( -\mathbf{U}^T \frac{\partial \mathbf{F}_{\text{int}}}{\partial \bar{m}_e^{(i)}} \right) + (1 - w) \frac{\bar{\rho}_e \hat{\gamma}_i v_e}{\sum_{k=1}^N v_k} + \frac{1}{N} \left( \left[ \lambda_e^{(n)} + \mu^{(n)} h_e^{(n)} \right] \frac{\partial h_e^{(n)}}{\partial \bar{m}_e^{(i)}} + \mathbf{\Lambda}^T \frac{\partial \mathbf{F}_{\text{int}}}{\partial \bar{m}_e^{(i)}} \right) \tag{B.7}$$

where the gradients of internal force  $\mathbf{F}_{int}$  with respect to the physical variables can be expressed for a linear material model using solid material stiffness matrices  $\mathbf{k}_{0,e}^{(i)}$  and the displacement vector  $\mathbf{u}_e$  for the

eth element as

$$\frac{\partial \mathbf{F}_{\text{int}}}{\partial \bar{\rho}_e} = [(1 - \epsilon) p_\rho \bar{\rho}_e^{p_\rho - 1}] \left( \sum_{i=1}^{N_m} (\bar{m}_e^{(i)})^{p_{\bar{e}}} \mathbf{k}_{0,e}^{(i)} \right) \mathbf{u}_e, \tag{B.8}$$

$$\frac{\partial \mathbf{F}_{\text{int}}}{\partial \bar{m}_{e}^{(i)}} = \left[\epsilon + (1 - \epsilon)\bar{\rho}_{e}^{p_{\rho}}\right] \left(p_{\xi}(\bar{m}_{e}^{(i)})^{p_{\xi}-1} \mathbf{k}_{0,e}^{(i)}\right) \mathbf{u}_{e},\tag{B.9}$$

and  $\Lambda$  is the adjoint vector obtained by solving the adjoint system

$$\mathbf{K}\Lambda = -\sum_{e=1}^{N} \left[ \lambda_e^{(n)} + \mu^{(n)} h_e^{(n)} \right] \frac{\partial h_e^{(n)}}{\partial \mathbf{U}}.$$
 (B.10)

The gradients of equality constraints  $h_e^{(n)}$  vanish when  $g_e^{(n)} < -(\lambda_e^{(n)}/\mu^{(n)})$ ; otherwise, they are computed through (superscript n is omitted hereafter because all the operations are carried out in same  $n^{\text{th}}$  AL step):

$$\frac{\partial h_e}{\partial \bar{\rho}_e} = \frac{\partial g_e}{\partial \bar{\rho}_e} = [(1 - \epsilon)p_\rho \bar{\rho}_e^{p_\rho - 1}](f_e^{(\xi)} - 1)((f_e^{(\xi)} - 1)^2 + 1) \tag{B.11}$$

$$\frac{\partial h_e}{\partial \bar{m}_e^{(i)}} = \frac{\partial g_e}{\partial \bar{m}_e^{(i)}} = [\epsilon + (1 - \epsilon) \bar{\rho}_e^{p_\rho}] (3(f_e^{(\xi)} - 1)^2 + 1) \frac{\partial f_e^{(\xi)}}{\partial \bar{m}_e^{(i)}}$$
(B.12)

$$\frac{\partial h_e}{\partial \mathbf{U}} = \frac{\partial g_e}{\partial \mathbf{U}} = [\epsilon + (1 - \epsilon)\bar{\rho}_e^{p_\rho}](3(f_e^{(\xi)} - 1)^2 + 1)\frac{\partial f_e^{(\xi)}}{\partial \mathbf{U}}$$
(B.13)

The gradients of  $f^{(\xi)}$  with respect to the physical material variables  $\bar{m}^{(i)}$  and state variable U are obtained for element e as

$$\frac{\partial f_e^{(\xi)}}{\partial \bar{m}_e^{(i)}} = p_{f_{\xi}} (\bar{m}_e^{(i)})^{p_{f_{\xi}} - 1} \eta^{(i)}, \tag{B.14}$$

$$\frac{\partial f_e^{(\xi)}}{\partial \mathbf{U}} = \sum_{i=1}^{N_m} (\bar{m}_e^{(i)})^{P_{f_{\xi}}} \frac{\partial \eta^{(i)}}{\partial \mathbf{U}},\tag{B.15}$$

$$\frac{\partial \eta^{(i)}}{\partial \mathbf{U}} = \left(\frac{\partial \eta^{(i)}}{\partial \sigma_1^{(i)}} \frac{\partial \sigma_1^{(i)}}{\partial \sigma_2^{(i)}} + \frac{\partial \eta^{(i)}}{\partial \sigma_2^{(i)}} \frac{\partial \sigma_2^{(i)}}{\partial \sigma^{(i)}} + \frac{\partial \eta^{(i)}}{\partial \sigma_{\epsilon}^{(i)}} \frac{\partial \sigma_6^{(i)}}{\partial \sigma^{(i)}}\right) \cdot \frac{\partial \boldsymbol{\sigma}^{(i)}}{\partial \mathbf{U}}$$
(B.16)

where  $\eta^{(i)}$  and  $\sigma^{(i)}$  are the load factor-based Tsai–Wu yield function and the Cauchy stress tensor for candidate material phase i, respectively. The sensitivities for von Mises yield function can be derived from the same expression as the von Mises yield function is identical to load factor-based Tsai–Wu yield function when isotropic strength parameters, i.e.,  $X_t = X_c = Y_t = Y_c = \sqrt{3}S = \bar{\sigma}_{\rm iso}$  are considered for the isotropic candidate material. The sensitivity of Cauchy stress tensor with respect to displacement vector is obtained as  $\frac{\partial \sigma^{(i)}}{\partial U} = \mathbb{C}^{(i)}\mathbf{B}^{(i)}$ , where  $\mathbb{C}^{(i)}$  is the solid material constitutive matrix and  $\mathbf{B}^{(i)}$  is the strain–displacement matrix of material phase i  $(i=1,\dots,N_m)$ .

#### Appendix C. Variation of compliance weight w

This study uses compliance weights w = 0.35 and w = 0.3 for the demonstrated examples. The choice of this weight factor w may be varied according to different design problem and requirements, and different additive manufacturing methods. Generally, the optimized solution uses more mass (equivalently volume, since mass densities are same for all material phases) to increase structural stiffness for a larger compliance weight w. Fig. C.9 presents a similar observation with Example 1 design problem and compliance weights w = 0.25, 0.50,and 0.75 for both topology optimization cases without and with stressconstraints. Moreover, optimization results without stress constraint show larger YFM, i.e., stress constraint violation for lower compliance weight. Since the optimized design with w = 0.25 uses the lowest material amount, the overall structural stiffness is lower compared to the other two cases. As a result, local strains increase for the same load amount, which leads to higher local stresses and YFM values. Hence, the importance of including anisotropic stress constraints becomes more evident for optimization cases with lower compliance weight, i.e., for manufacturing lightweight optimized structures.

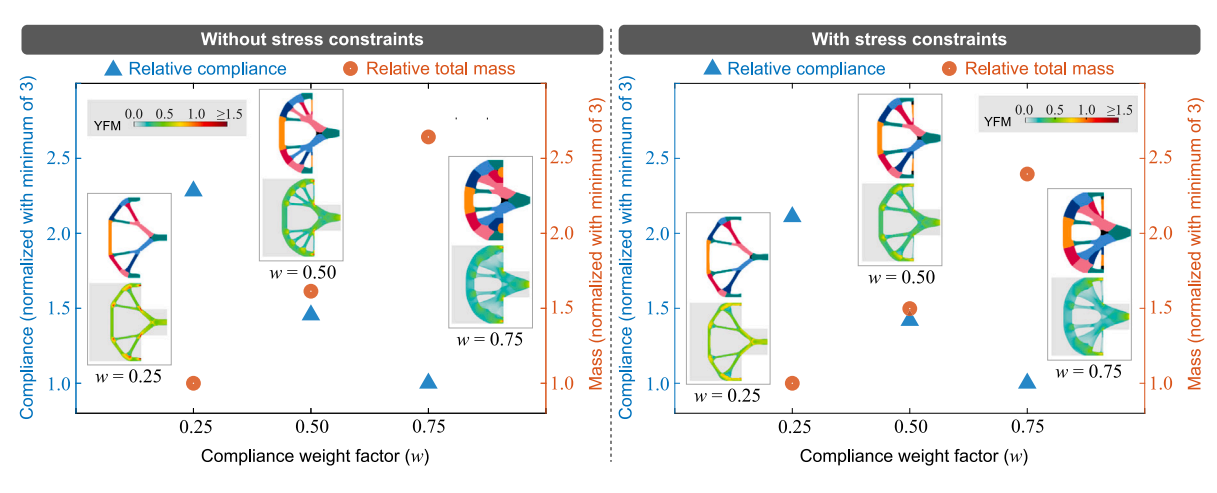


Fig. C.9. Effect of compliance weight factor w on optimized designs for without stress constraint (left) and with stress constraints (right).

#### References

- M.P. Bendsøe, O. Sigmund, Topology Optimization: Theory, Methods and Applications, Springer, Berlin, Heidelberg, 2003, http://dx.doi.org/10.1007/978-3-662-05086-6.
- [2] C. Wang, Z. Zhao, M. Zhou, O. Sigmund, X.S. Zhang, A comprehensive review of educational articles on structural and multidisciplinary optimization, Struct. Multidiscip. Optim. 64 (5) (2021) 2827–2880, http://dx.doi.org/10.1007/s00158-021-03050-7
- [3] L. Zhang, Q. Ma, J. Ding, S. Qu, J. Fu, M.W. Fu, X. Song, M.Y. Wang, Design of elastically isotropic shell lattices from anisotropic constitutive materials for additive manufacturing, Addit. Manuf. 59 (2022) 103185, http:// dx.doi.org/10.1016/j.addma.2022.103185, URL https://www.sciencedirect.com/ science/article/pii/S2214860422005747.
- [4] S.-H. Ahn, M. Montero, D. Odell, S. Roundy, P.K. Wright, Anisotropic material properties of fused deposition modeling ABS, Rapid Prototyp. J. 8 (4) (2002) 248–257, http://dx.doi.org/10.1108/13552540210441166.
- [5] S.H. Ahn, C. Baek, S. Lee, I.S. Ahn, Anisotropic tensile failure model of rapid prototyping parts - fused deposition modeling (FDM), Internat. J. Modern Phys. B 17 (08n09) (2003) 1510–1516, http://dx.doi.org/10.1142/S0217979203019241.
- [6] C. Ziemian, M. Sharma, S. Ziemian, Anisotropic mechanical properties of ABS parts fabricated by fused deposition modelling, in: M. Gokcek (Ed.), Mechanical Engineering, IntechOpen, Rijeka, 2012, http://dx.doi.org/10.5772/34233.
- [7] N. Hill, M. Haghi, Deposition direction-dependent failure criteria for fused deposition modeling polycarbonate, Rapid Prototyp. J. 20 (3) (2014) 221–227, http://dx.doi.org/10.1108/RPJ-04-2013-0039.
- [8] B. Huang, S. Singamneni, Raster angle mechanics in fused deposition modelling, J. Compos. Mater. 49 (3) (2015) 363–383, http://dx.doi.org/10.1177/0021998313519153.
- [9] J.C. Riddick, M.A. Haile, R.V. Wahlde, D.P. Cole, O. Bamiduro, T.E. Johnson, Fractographic analysis of tensile failure of acrylonitrile-butadiene-styrene fabricated by fused deposition modeling, Addit. Manuf. 11 (2016) 49–59, http:// dx.doi.org/10.1016/j.addma.2016.03.007, URL https://www.sciencedirect.com/ science/article/pii/S2214860416300410.
- [10] C. Yang, X. Tian, T. Liu, Y. Cao, D. Li, 3D printing for continuous fiber reinforced thermoplastic composites: mechanism and performance, Rapid Prototyp. J. 23 (1) (2017) 209–215, http://dx.doi.org/10.1108/RPJ-08-2015-0098.
- [11] A. Grant, B. Regez, S. Kocak, J.D. Huber, A. Mooers, Anisotropic properties of 3-D printed poly lactic acid (PLA) and acrylonitrile butadiene styrene (ABS) plastics, Results Mater. 12 (2021) 100227, http://dx.doi.org/10.1016/j.rinma.2021.100227, URL https://www.sciencedirect.com/science/article/pii/S2590048X21000601.
- [12] P. Zhang, J. Liu, A.C. To, Role of anisotropic properties on topology optimization of additive manufactured load bearing structures, Scr. Mater. 135 (2017) 148–152, http://dx.doi.org/10.1016/j.scriptamat.2016.10.021, URL https://www.sciencedirect.com/science/article/pii/S1359646216305164.
- [13] J. Liu, A.T. Gaynor, S. Chen, Z. Kang, K. Suresh, A. Takezawa, L. Li, J. Kato, J. Tang, C.C.L. Wang, L. Cheng, X. Liang, A.C. To, Current and future trends in topology optimization for additive manufacturing, Struct. Multidiscip. Optim. 57 (6) (2018) 2457–2483, http://dx.doi.org/10.1007/s00158-018-1994-3.
- [14] C. Koch, L. Van Hulle, N. Rudolph, Investigation of mechanical anisotropy of the fused filament fabrication process via customized tool path generation, Addit. Manuf. 16 (2017) 138–145, http://dx.doi.org/10.1016/j.addma.2017.06.003, URL https://www.sciencedirect.com/science/article/pii/S2214860417300465.

- [15] H. Zhang, D. Yang, Y. Sheng, Performance-driven 3D printing of continuous curved carbon fibre reinforced polymer composites: A preliminary numerical study, Composites B 151 (2018) 256–264, http://dx.doi.org/10.1016/j. compositesb.2018.06.017, URL https://www.sciencedirect.com/science/article/ pii/S1359836818305274.
- [16] G. Fang, T. Zhang, S. Zhong, X. Chen, Z. Zhong, C.C.L. Wang, Reinforced FDM: Multi-axis filament alignment with controlled anisotropic strength, ACM Trans. Graph. 39 (6) (2020) http://dx.doi.org/10.1145/3414685.3417834.
- [17] L. Xia, S. Lin, G. Ma, Stress-based tool-path planning methodology for fused fil-ament fabrication, Addit. Manuf. 32 (2020) 101020, http://dx.doi.org/10.1016/j.addma.2019.101020, URL https://www.sciencedirect.com/science/article/pii/S2214860419315659.
- [18] T. Suzuki, S. Fukushige, M. Tsunori, Load path visualization and fiber trajectory optimization for additive manufacturing of composites, Addit. Manuf. 31 (2020) 100942, http://dx.doi.org/10.1016/j.addma.2019.100942, URL https://www.sciencedirect.com/science/article/pii/\$2214860419311030.
- [19] V. Murugan, G. Alaimo, F. Auricchio, S. Marconi, An orientation-field based algorithm for free-form material extrusion, Addit. Manuf. 59 (2022) 103064, http://dx.doi.org/10.1016/j.addma.2022.103064, URL https://www.sciencedirect.com/science/article/pii/S2214860422004560.
- [20] X. Chen, G. Fang, W.-H. Liao, C.C. Wang, Field-based toolpath generation for 3D printing continuous fibre reinforced thermoplastic composites, Addit. Manuf. 49 (2022) 102470, http://dx.doi.org/10.1016/j.addma.2021.102470, URL https://www.sciencedirect.com/science/article/pii/S2214860421006205.
- [21] T. Liu, S. Yuan, Y. Wang, Y. Xiong, J. Zhu, L. Lu, Y. Tang, Stress-driven infill mapping for 3D-printed continuous fiber composite with tunable infill density and morphology, Addit. Manuf. 62 (2023) 103374, http://dx.doi.org/10.1016/j.addma.2022.103374, URL https://www.sciencedirect.com/science/article/pii/S2214860422007631.
- [22] R. Hoglund, D. Smith, Continuous fiber angle topology optimization for polymer fused fillament fabrication, 2016, URL https://hdl.handle.net/2152/89657.
- [23] J. Liu, H. Yu, Concurrent deposition path planning and structural topology optimization for additive manufacturing, Rapid Prototyp. J. 23 (5) (2017) 930–942, http://dx.doi.org/10.1108/RPJ-05-2016-0087.
- [24] C. Dapogny, R. Estevez, A. Faure, G. Michailidis, Shape and topology optimization considering anisotropic features induced by additive manufacturing processes, Comput. Methods Appl. Mech. Engrg. 344 (2019) 626–665, http://dx.doi.org/10.1016/j.cma.2018.09.036, URL https://www.sciencedirect.com/science/article/pii/S0045782518304894.
- [25] S. Li, S. Yuan, J. Zhu, C. Wang, J. Li, W. Zhang, Additive manufacturing-driven design optimization: Building direction and structural topology, Addit. Manuf. 36 (2020) 101406, http://dx.doi.org/10.1016/j.addma.2020.101406, URL https://www.sciencedirect.com/science/article/pii/S2214860420307788.
- [26] J. Lee, C. Kwon, J. Yoo, S. Min, T. Nomura, E.M. Dede, Design of spatially-varying orthotropic infill structures using multiscale topology optimization and explicit de-homogenization, Addit. Manuf. 40 (2021) 101920, http://dx.doi.org/10.1016/j.addma.2021.101920, URL https://www.sciencedirect.com/science/article/pii/S2214860421000853.
- [27] M. Bi, P. Tran, L. Xia, G. Ma, Y.M. Xie, Topology optimization for 3D concrete printing with various manufacturing constraints, Addit. Manuf. 57 (2022) 102982, http://dx.doi.org/10.1016/j.addma.2022.102982, URL https://www.sciencedirect.com/science/article/pii/S221486042200375X.
- [28] T. Shafighfard, T.A. Cender, E. Demir, Additive manufacturing of compliance optimized variable stiffness composites through short fiber alignment along curvilinear paths, Addit. Manuf. 37 (2021) 101728, http://dx.doi.org/10.1016/ j.addma.2020.101728, URL https://www.sciencedirect.com/science/article/pii/ S2214860420311003.

- [29] R.R. Fernandes, N. van de Werken, P. Koirala, T. Yap, A.Y. Tamijani, M. Tehrani, Experimental investigation of additively manufactured continuous fiber reinforced composite parts with optimized topology and fiber paths, Addit. Manuf. 44 (2021) 102056, http://dx.doi.org/10.1016/j.addma.2021.102056, URL https://www.sciencedirect.com/science/article/pii/S2214860421002219.
- [30] F.V. Senhora, O. Giraldo-Londoño, I.F.M. Menezes, G.H. Paulino, Topology optimization with local stress constraints: a stress aggregation-free approach, Struct. Multidiscip. Optim. 62 (4) (2020) 1639–1668, http://dx.doi.org/10.1007/ s00158-020-02573-9.
- [31] O. Giraldo-Londoño, G.H. Paulino, PolyStress: A matlab implementation for local stress-constrained topology optimization using the augmented Lagrangian method, Struct. Multidiscip. Optim. 63 (4) (2021) 2065–2097, http://dx.doi.org/ 10.1007/s00158-020-02760-8.
- [32] Y. Luo, Z. Kang, Topology optimization of continuum structures with Drucker– Prager yield stress constraints, Comput. Struct. 90–91 (2012) 65–75, http://dx. doi.org/10.1016/j.compstruc.2011.10.008, URL https://www.sciencedirect.com/ science/article/pii/S0045794911002550.
- [33] O. Giraldo-Londoño, G.H. Paulino, A unified approach for topology optimization with local stress constraints considering various failure criteria: von mises, Drucker-Prager, tresca, mohr-Coulomb, bresler- pister and willam-warnke, Proc. R. Soc. A.4762019086120190861 (2020) http://dx.doi.org/10.1098/rspa.2019. 0861
- [34] R.D. Kundu, W. Li, X.S. Zhang, Multimaterial stress-constrained topology optimization with multiple distinct yield criteria, Extreme Mech. Lett. 54 (2022) 101716, http://dx.doi.org/10.1016/j.eml.2022.101716, URL https:// www.sciencedirect.com/science/article/pii/S2352431622000657.
- [35] J. Liu, J. Yan, H. Yu, Stress-constrained topology optimization for material extrusion polymer additive manufacturing, J. Comput. Des. Eng. 8 (3) (2021) 979–993, http://dx.doi.org/10.1093/jcde/qwab028, arXiv:https://academic.oup. com/jcde/article-pdf/8/3/979/38487930/qwab028.pdf.
- [36] E. Ulu, E. Korkmaz, K. Yay, O. Burak Ozdoganlar, L. Burak Kara, Enhancing the structural performance of additively manufactured objects through build orientation optimization, J. Mech. Des. 137 (11) (2015) http://dx.doi.org/10.1115/1.4030998, 111410, arXiv:https://asmedigitalcollection.asme.org/mechanicaldesign/article-pdf/137/11/111410/6227988/md\_137\_11\_111410.pdf.
- [37] N. Umetani, R. Schmidt, Cross-sectional structural analysis for 3D printing optimization, in: SIGGRAPH Asia 2013 Technical Briefs, SA '13, Association for Computing Machinery, New York, NY, USA, 2013, http://dx.doi.org/10.1145/ 2542355.2542361.
- [38] Y. Wang, S. Li, Y. Yu, Y. Xin, X. Zhang, Q. Zhang, S. Wang, Lattice structure design optimization coupling anisotropy and constraints of additive manufacturing, Mater. Des. 196 (2020) 109089, http://dx.doi.org/10.1016/ j.matdes.2020.109089, URL https://www.sciencedirect.com/science/article/pii/ S0264127520306249.
- [39] A.M. Mirzendehdel, B. Rankouhi, K. Suresh, Strength-based topology optimization for anisotropic parts, Addit. Manuf. 19 (2018) 104–113, http://dx.doi.org/10.1016/j.addma.2017.11.007, URL https://www.sciencedirect.com/science/article/pii/S2214860416303475.
- [40] J. Zou, X. Xia, Topology optimization for additive manufacturing with strength constraints considering anisotropy, J. Comput. Des. Eng. 10 (2) (2023) 892–904, http://dx.doi.org/10.1093/jcde/qwad028, arXiv:https://academic.oup.com/jcde/ article-pdf/10/2/892/50063156/qwad028.pdf.
- [41] G. Ma, W. Yang, L. Wang, Strength-constrained simultaneous optimization of topology and fiber orientation of fiber-reinforced composite structures for additive manufacturing, Adv. Struct. Eng. 25 (7) (2022) 1636–1651, http://dx. doi.org/10.1177/13694332221088946, arXiv:10.1177/13694332221088946.
- [42] M. Eckrich, P.A. Arrabiyeh, A.M. Dlugaj, D. May, Structural topology optimization and path planning for composites manufactured by fiber placement technologies, Compos. Struct. 289 (2022) 115488, http://dx.doi.org/10.1016/ j.compstruct.2022.115488, URL https://www.sciencedirect.com/science/article/ pii/S0263822322002793.
- [43] Y. Zhou, T. Nomura, K. Saitou, Multicomponent topology optimization for additive manufacturing with build volume and cavity free constraints, J. Comput. Inf. Sci. Eng. 19 (2) (2019) http://dx.doi.org/10.1115/1.4042640, 021011, arXiv:https://asmedigitalcollection.asme.org/computingengineering/articlepdf/19/2/021011/5998483/icise 019 02 021011.pdf.
- [44] Y. Zhou, T. Nomura, K. Saitou, Anisotropic multicomponent topology optimization for additive manufacturing with build orientation design and stress-constrained interfaces, J. Comput. Inf. Sci. Eng. 21 (1) (2020) http://dx.doi.org/10.1115/1.4047487, 011007, arXiv:https://asmedigitalcollection.asme.org/computingengineering/article-pdf/21/1/011007/6613566/jcise\_21\_1\_011007.pdf.
- [45] R.D. Kundu, X.S. Zhang, Stress-based topology optimization for fiber composites with improved stiffness and strength: Integrating anisotropic and isotropic materials, Compos. Struct. 320 (2023) 117041, http://dx.doi.org/10.1016/ j.compstruct.2023.117041, URL https://www.sciencedirect.com/science/article/ pii/S0263822323003859.
- [46] M.P. Bendsøe, O. Sigmund, Material interpolation schemes in topology optimization, Arch. Appl. Mech. 69 (9) (1999) 635–654, http://dx.doi.org/10.1007/s004190050248.

- [47] O. Sigmund, Design of multiphysics actuators using topology optimization Part II: Two-material structures, Comput. Methods Appl. Mech. Engrg. 190 (49) (2001) 6605–6627, http://dx.doi.org/10.1016/S0045-7825(01)00252-3.
- [48] T.E. Bruns, D.A. Tortorelli, Topology optimization of non-linear elastic structures and compliant mechanisms, Comput. Methods Appl. Mech. Engrg. 190 (26) (2001) 3443–3459, http://dx.doi.org/10.1016/S0045-7825(00)00278-4.
- [49] B. Bourdin, Filters in topology optimization, Internat. J. Numer. Methods Engrg. 50 (9) (2001) 2143–2158, http://dx.doi.org/10.1002/nme.116.
- [50] O. Sigmund, Morphology-based black and white filters for topology optimization, Struct. Multidiscip. Optim. 33 (4) (2007) 401–424, http://dx.doi.org/10.1007/ s00158-006-0087-x.
- [51] F. Wang, B.S. Lazarov, O. Sigmund, On projection methods, convergence and robust formulations in topology optimization, Struct. Multidiscip. Optim. 43 (6) (2011) 767–784, http://dx.doi.org/10.1007/s00158-010-0602-y.
- [52] Y. Zhou, T. Nomura, K. Saitou, Multi-component topology and material orientation design of composite structures (MTO-C), Comput. Methods Appl. Mech. Engrg. 342 (2018) 438–457, http://dx.doi.org/10.1016/j.cma.2018.07.039.
- [53] M.P. Bendsøe, O. Sigmund, Topology Optimization: Theory, Methods, and Applications, Springer, Berlin, Germany, 2003, p. 370.
- [54] M. Zhou, G. Rozvany, The COC algorithm, Part II: Topological, geometrical and generalized shape optimization, Comput. Methods Appl. Mech. Engrg. 89 (1–3) (1991) 309–336.
- [55] O. Sigmund, S. Torquato, Design of materials with extreme thermal expansion using a three-phase topology optimization method, J. Mech. Phys. Solids 45 (6) (1997) 1037–1067, http://dx.doi.org/10.1016/S0022-5096(96)00114-7.
- [56] W. Li, F. Wang, O. Sigmund, X.S. Zhang, Design of composite structures with programmable elastic responses under finite deformations, J. Mech. Phys. Solids 151 (2021) 104356, http://dx.doi.org/10.1016/j.jmps.2021.104356, URL https://www.sciencedirect.com/science/article/pii/S0022509621000533.
- [57] A.A. Groenwold, R.T. Haftka, Optimization with non-homogeneous failure criteria like Tsai–Wu for composite laminates, Struct. Multidiscipl. Optim. 32 (3) (2006) 183–190, http://dx.doi.org/10.1007/s00158-006-0020-3.
- [58] S.W. Tsai, E.M. Wu, A general theory of strength for anisotropic materials, J. Compos. Mater. 5 (1) (1971) 58–80, http://dx.doi.org/10.1177/002199837100500106, arXiv:10.1177/002199837100500106.
- [59] R.v. Mises, Mechanik der festen körper im plastisch- deformablen zustand, Nachrichten von der Gesellschaft Wiss. zu Göttingen, Math.-Phys. Kl. 4 (1913) 582–592, URL http://eudml.org/doc/58894.
- [60] D.P. Bertsekas, Nonlinear Programming, Athena Scientific, Belmont, MA, 1999.
- [61] J. Nocedal, S. Wright, Numerical Optimization, Springer, New York, NY, 2006, http://dx.doi.org/10.1007/978-0-387-40065-5.
- [62] J. Pereira, E. Fancello, C. Barcellos, Topology optimization of continuum structures with material failure constraints, Struct. Multidiscip. Optim. 26 (1-2) (2004) 50-66
- [63] E.A. Fancello, Topology optimization for minimum mass design considering local failure constraints and contact boundary conditions, Struct. Multidiscip. Optim. 32 (3) (2006) 229–240, http://dx.doi.org/10.1007/s00158-006-0019-9.
- [64] H. Emmendoerfer, E.A. Fancello, A level set approach for topology optimization with local stress constraints, Internat. J. Numer. Methods Engrg. 99 (2) (2014) 129–156
- [65] H. Emmendoerfer, E.A. Fancello, Topology optimization with local stress constraint based on level set evolution via reaction-diffusion, Comput. Methods Appl. Mech. Engrg. 305 (2016) 62–88.
- [66] H. Emmendoerfer, E.C.N. Silva, E.A. Fancello, Stress-constrained level set topology optimization for design-dependent pressure load problems, Comput. Methods Appl. Mech. Engrg. 344 (2019) 569–601, http://dx.doi.org/10. 1016/j.cma.2018.10.004, URL https://www.sciencedirect.com/science/article/ pii/S0045782518305000.
- [67] G.A. da Silva, A.T. Beck, E.L. Cardoso, Topology optimization of continuum structures with stress constraints and uncertainties in loading, Internat. J. Numer. Methods Engrg. 113 (1) (2018) 153–178, http://dx.doi.org/10.1002/nme.5607, arXiv:https://onlinelibrary.wiley.com/doi/pdf/10.1002/nme.5607, URL https://onlinelibrary.wiley.com/doi/abs/10.1002/nme.5607.
- [68] G.A. da Silva, A.T. Beck, O. Sigmund, Stress-constrained topology optimization considering uniform manufacturing uncertainties, Comput. Methods Appl. Mech. Engrg. 344 (2019) 512–537, http://dx.doi.org/10.1016/j.cma.2018.10.020, URL https://www.sciencedirect.com/science/article/pii/S0045782518305231.
- [69] P. Duysinx, O. Sigmund, New Developments in Handling Stress Constraints in Optimal Material Distribution, in: 7th AIAA/USAF/NASA/ISSMO Symposium on Multidisciplinary Analysis and Optimization, American Institute of Aeronautics and Astronautics, 1998, http://dx.doi.org/10.2514/6.1998-4906, 0.
- [70] C. Dudescu, L. Racz, Effects of raster orientation, infill rate and infill pattern on the mechanical properties of 3D printed materials, Acta Univ. Cibiniensis. Tech. Ser. 69 (1) (2017) 23–30, http://dx.doi.org/10.1515/aucts-2017-0004.
- [71] S. Rodríguez-Reyna, C. Mata, J. Díaz-Aguilera, H. Acevedo-Parra, F. Tapia, Mechanical properties optimization for PLA, ABS and nylon + CF manufactured by 3D FDM printing, Mater. Today Commun. 33 (2022) 104774, http://dx. doi.org/10.1016/j.mtcomm.2022.104774, URL https://www.sciencedirect.com/ science/article/pii/S2352492822016154.

- [72] J. Blaber, B. Adair, A. Antoniou, Ncorr: Open-source 2D digital image correlation matlab software, Exp. Mech. 55 (6) (2015) 1105–1122, http://dx.doi.org/10. 1007/s11340-015-0009-1.
- [73] K. Svanberg, The method of moving asymptotes—A new method for structural optimization, Internat. J. Numer. Methods Engrg. 24 (2) (1987) 359–373, http: //dx.doi.org/10.1002/nme.1620240207.
- [74] X.S. Zhang, H. Chi, Z. Zhao, Topology optimization of hyperelastic structures with anisotropic fiber reinforcement under large deformations, Comput. Methods Appl. Mech. Engrg. 378 (2021) 113496, http://dx.doi.org/10.1016/j.cma.2020.113496, URL https://www.sciencedirect.com/science/article/pii/S0045782520306812.